ABSTRACT

Cu/BN_x CATALYSTS FOR ELECTROCATALYTIC REDUCTION OF NITROGEN AND NITRATE WASTE

by
Siming Huo

Ammonia (NH_3) is one of the most important chemicals to the whole human society. The invention of the Haber-Bosch process enabled the industrial production of NH_3. However, owing to the high capital costs of the centralized plant and the equipment and the negative environmental impact, it is no longer suitable for today's needs of human development. As a result, there is an urgent need to investigate sustainable approaches for ammonia production. Among those reported studies, nitrogen reduction (NRR) and nitrate reduction reaction (NO_3RR) are considered applicable in the future. However, after decades of studying them for years, the catalysts are still suffering from limited activity.

The main objective of this study is to develop a series of promising transition metal based single atom catalysts for NRR and NO_3RR. For the stabilization of metal atoms as the single atomic sites, porous boron nitride (BN_x) is used as the substrate. Catalysts with tuned metal loading and substrate porosity are synthesized by controlling the content of precursors in the synthesis process. First, different metals are screened for the optimized NH_3 productivity and obtain the highest NH_3 productivity of 118.3μg /h/mg_{cat} in NRR is obtained on the $CuBN_x$ catalysts. Then the $CuBN_x$ catalysts are studied in NO_3RR to further improve the NH_3 yield. The Lewis acidity and interaction between boron atoms and Cu atoms are the origin of the promising activity.

Meanwhile, the catalysts are investigated using X-ray Absorption Spectroscopy (XAS), the XAS results confirm the formation of Cu single atomic sites by bonding with BNx. With XAS and H_2 temperature programmed reduction, we prove the preference of higher oxidation states of Cu for NO_3RR. Thus, O_2 plasma is used to further improve the NH_3 production rate by increasing the oxidation state of Cu atoms of the single atomic sites. The highest NH_3 productivity in this work obtained is 4029 $\mu g/h/mg_{cat}$ which is currently the highest productivity ever reported. A systemic study with different plasma treatment further confirms the interaction between Cu, BN and O species plays a key role for NRR and NO_3RR . However, a thorough understanding of the Cu-BNx-O system, and NRR and NO_3RR reaction mechanisms are required for the future work in order to further improve NH_3 productivity.

Cu/BN_x CATALYSTS FOR ELECTROCATALYTIC REDUCTION OF NITROGEN AND NITRATE WASTE

by
Siming Huo

A Dissertation
Submitted to the Faculty of
New Jersey Institute of Technology
in Partial Fulfillment of the Requirements for the Degree of
Doctor of Philosophy in Chemical Engineering

Otto H. York Department of Chemical and Materials Engineering

May 2023

.

APPROVAL PAGE

Cu/BN_x CATALYSTS FOR ELECTROCATALYTIC REDUCTION OF NITROGEN AND NITRATE WASTE

Siming Huo

Dr. Xianqin Wang, Dissertation Advisor — Date
Professor of Chemical and Materials Engineering, NJIT

Dr. Xiaoyang Xu, Committee Member — Date
Associate Professor of Chemical and Materials Engineering, NJIT

Dr. Joshua Young, Committee Member — Date
Assistant Professor of Chemical and Materials Engineering, NJIT

Dr. Mengqiang Zhao, Committee Member — Date
Assistant Professor of Chemical and Materials Engineering, NJIT

Dr. Zafar Iqbal, Committee Member — Date
Research Professor Emeritus of Chemistry and Environmental Science, NJIT

BIOGRAPHICAL SKETCH

Author: Siming Huo

Degree: Doctor of Philosophy

Date: May 2023

Undergraduate and Graduate Education:

- Doctor of Philosophy in Chemical Engineering,
  New Jersey Institute of Technology, Newark, NJ, 2023

- Master of Engineering in Chemical Engineering,
  University at Buffalo, Buffalo, NY. USA, 2019

- Bachelor of Science in Chemical Engineering and Technology,
  Central South University, Changsha, P. R. China, 2017

Major: Chemical Engineering

Presentations and Publications:

Huo, S., Lu, J., & Wang, X. (2021). Electrodeposition of Ni on MWNTs as a promising catalyst for CO2RR. Energy Science and Engineering, 9(7), 1042-1047.

Huo, S., Lu, J., & Wang, X. (2022). Recent progress in electrochemical reduction of carbon dioxide on metal single-atom catalysts. Energy Science and Engineering, 10(5), 1584-1600.

Zhuang, H., Huo, S., Alzaim, S., Iqbal, Z., Ravindra, N. M., & Wang, X. (2022). Synthesis of polymeric nitrogen with non-thermal radio frequency plasma. Catalysis Today.

ACKNOWLEDGMENT

Special thanks are given to my advisor, Professor Xianqin Wang for her insightful supervision, encouragement, and support throughout my PhD study.

I would like to thank the members of my Committee, Dr. Xiaoyang Xu, Dr. Joshua Young, Dr. Menqian Zhao and Dr. Zafa Iqbal, for their time reading my dissertation, attending my defense, and providing valuable comments. I would also like to thank Dr. Young for the support for doing computational research and Dr. Zhao and Dr. Xu for instrument usage.

This work was supported by a National Science Foundation grant (CBET-1804949). I would also like to thank the Department of Chemical and Materials Engineering for supporting my graduate studies.

I would like to thank Dr. Tao Li at North Illinois University for the great support on XAS data collection. I appreciate the staff, especially Shawn Yetman, at NJIT for his technical support.

My thanks to my past group members: Dr. Haizheng Zhuang and Dr. Alzaim Safa for their help and support. I am also grateful to Mo Li for her help and coaching in computational research.

Last but not least, my greatest thank to my parents and Jessica Wang for their love, support and understanding through my life.

TABLE OF CONTENTS

TABLE OF CONTENTS
(Continued)

Chapter **Page**

TABLE OF CONTENTS

(Continued)

Chapter **Page**

LIST OF TABLES

LIST OF FIGURES

LIST OF FIGURES
(Continued)

CHAPTER 1

BACKGROUND AND OBJECTIVES

1.1 Background

Development of state-of-the-art catalysts plays a critical role in the fields of chemical engineering for efficient energy conversion and environmental protection. Although some excellent catalysts have been developed, challenges of further improvement of performance and environmental protection remain. Therefore, metal single-atom catalysts (M-SACs), a class of catalysts in which catalytically active individual and isolated metal atoms are anchored to supports, have emerged as a novel class of catalysts that can exhibit optimal metal utilization, with all metal atoms being exposed to reactants and available for catalytic reactions[1, 2]. Furthermore, the unique properties of M-SACs have attracted great attention from researchers due to distinct behaviors in comparison with metal nanoparticles (MNPs) and nonmetal catalysts in which extraordinary catalytic activity, selectivity and stability for various reactions including CO oxidation[3, 4], water splitting[5], electroreduction of CO_2[6-8], oxygen reduction reaction (ORR)[9, 10] nitrogen reduction reaction (NRR)[11] and nitrate reduction reaction (NO_3RR)[12].

1.1.1 Metal Based Catalysts

Metal nanoparticles (MNPs) are of high scientific interest, as they show unusual properties compared to their bulk counterparts. At the nanoscale, the properties of the materials generally change. The effect that causes changes in the properties of the

materials is referred to as the size-induced effect[13]. As the size of a material decreases in the nonorange, the percentage of atoms at its surface becomes substantial. Therefore, the subsequent surface-to-volume ratio increases substantially, which influences the surface-related properties of the material. In general, the interesting properties and the advantageous characteristics of NPs are:

High surface-to-volume ratios, which provide a large number of active sites per unit area compared to their bulk counterparts; higher zeta potential[14], averting the aggregation of nanoclusters in solution and possible separation and recyclability, reducing the probability of contamination of the catalyst with the product and making them cost-effective[15].

Transition M-NPs are clusters comprising from tens to thousands transition metal atoms. Their sizes vary between one nanometer to hundreds of nanometers in diameter. However, in catalysis, the most active is only of few nanometers[13]. The size of the M-NP catalysts is therefore a crucial aspect of the catalytic steps. Modern transition M-NPs (1–10 nm in diameter) differ from classical colloids (typically > 10 nm in diameter) in several aspects, including size and stability in solution[15, 16].

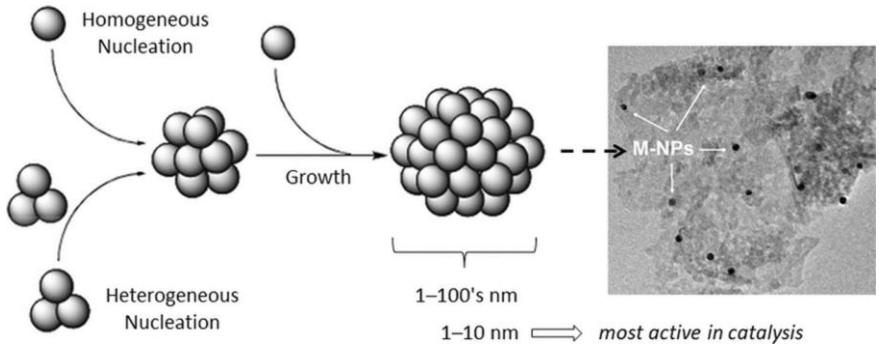

Figure 1.1 The growth of nanoparticles[15].

Due to their unusual properties based on their intrinsic large surface-to-volume ratios, transition M-NPs with narrow size distribution have gained strong interest in scientific research as well as industrial applications[17]. Transition MNPs are awarded with various features of an efficient catalyst. Colloidal MNPs as catalysts are used in homogeneous systems or otherwise can be heterogenized using a support such as alumina, silica, titania, carbon materials or zeolite[18, 19]. The support can be either a powder or a pre-shaped cheap solid with a high surface area that usually shows no catalytic activity on its own[20].

For example, transition metals at nanometer-sized dimensions shows notable activity in various applications from material to medicine. Due to its easy availability, low cost and environmentally friendly character, transition metals has received more consideration in different research areas including CO_2RR[21, 22], ORR[23, 24], NRR[25, 26] and other industrial applications[27-29].

For example, Zhang et al.[30]. used a two-step self-template conversion method to assemble NiO porous nanoplates on Co_3O_4 nanotubes to synthesize Co3O4@NiO HNT at the cathode through electrochemical NO_3RR to achieve an NH_3 yield of 6.93 mmol/h/g_{cart}, a selectivity of 62.29% and a Faraday efficiency of 54.97%[30]. Besides, Cu nanoparticles were widely investigated in CO_2RR[22, 31]. Recent studies proved that the selectivity and Faradic Efficiency (FE) of various products depends on the size of the particles. For instance, Manthiram et al.[31]. showed improved methane production over 7 nm Cu nanoparticles at overpotentials of −0.95 and −1.45 V vs. RHE when compared to polycrystalline Cu[31].

1.1.2 Non-metal based catalysts.

Metal-free catalysts are newly emerging green catalytic materials that have attracted much attention in recent years for their advantages of high efficiency, environment friendliness and economy in many industrial catalytic processes[32]. There are a variety of organic metal-free catalysts, which have been widely used in various homogeneous organic reactions for rearrangement reactions[33], cycloaddition[34], condensation, alkylation and carbonylation[35]. An important type of inorganic metal-free catalysts developed in recent years are nanocarbon materials that have demonstrated superior catalytic performance to traditional metal catalysts in many fields, including hydrocarbon conversion[34, 36], fine chemicals production[37], fuel cells[38, 39], and solar energy[40]. Metal-free carbon-based catalysis has become one of the most promising research directions in nanomaterials and catalysis. The carbon material itself is used as the catalyst and no metal is loaded or added, so the active sites for the reaction are the defective structure or functional groups on the carbon surface[41]. Compared with a metal-based catalyst, a nanocarbon catalyst has the advantages of low cost, no heavy metal pollution and environmental friendliness, while showing high selectivity and long-term stability under mild conditions in many catalytic processes[42].

For example, Robert Schlögl's research group carried out the oxidative dehydrogenation (ODH) of ethylbenzene using carbon nanofibers as the catalyst[43] and found that the carbon nanofibers showed a higher catalytic activity than highly dispersed graphite at the reaction temperature of 547 °C, and also had a far superior stability to traditional amorphous carbon black[44]. A series of studies subsequently

demonstrated that many nanostructured carbons can efficiently catalyze the ODH reaction of ethylbenzene to styrene, and that these catalysts exhibited comparable or even better activities than the traditional iron oxide catalysts[45]. Besides, the metal-free catalysts were widely used in other applications including ORR[46], CO_2RR[47], NRR[48] and NO_3RR[49]. The excellent catalytic performance of nanocarbon materials is due to their unique properties. First, most nanocarbons with a nano graphite structure possess good electrical conductivity and ability to store/release electrons, which facilitates the rate of electron transfer in the critical step of the catalytic reaction and increases the overall reaction rate[50]. Second, nanocarbon materials have very high specific surface areas and mesopore volumes and have more surface active-sites than conventional materials, thus improving the catalytic performance by the faster diffusion of reactant molecules in the mesopores[51].

Besides the nano carbon-based catalyst, boron nitride (BN) attracted much more attention. Recently, two pioneering works demonstrated that nitrogen could be fixed and reduced by non-metallic catalysts based on the boron atom, providing a new strategy for NRR catalysts[52, 53]. BN materials, especially boron nitride nanotubes (BNNTs), have was considered as potential candidates for heterogeneous catalysis because of BN's structural similarity to graphene. A boron anti-site(BAS) can be created on the BNNTs, if one of the N atoms is replaced with a B atom, which has been found to be an effective site for N_2 activation by using DFT investigations[54]. Similarly, DFT calculations also suggested that ammonia can be synthesized from nitrogen reduction on the 2D boron monolayer, wherein the N_2 adsorption is realized through

the electron transfer of boron and the first protonation is the rate-determining step[55]. Sun's group confirmed this possibility through experimental results that boron nanosheet (BNS) is proposed as an elemental two-dimensional (2D) material to effectively catalyze the NRR toward NH_3 synthesis with excellent selectivity. When tested in 0.1 M Na_2SO_4, such BNS catalyst attains a high Faradaic efficiency of 4.04% and a large NH3 yield of 13.22 μg/h/mg_{cat} at −0.80 V vs reversible hydrogen electrode (RHE), with strong electrochemical durability. Density functional theory calculations suggest that the B atoms of both oxidized and H-deactivated BNS can catalyze the NRR more effectively than clean BNS, and the rate-determining step is the desorption process of the second NH_3 gas[56]. The boron atoms were considered as the active sites in the reaction[56, 57].

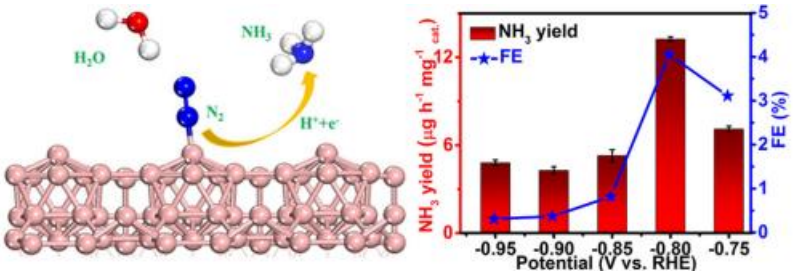

Figure 1.2 The DFT simulation of NRR on BNS and the catalytic performance[56].

1.1.3 Metal Single Atom Catalysts

Although metal-based catalysts have been reported for promising activity in various applications, the performance still required further improvement for commercialization. In addition, due to the nature of the metal particles and clusters, the accessibility of

active sites on the surface of nanoparticles are limited, thus one strategy to achieve high specific activity is the reductions in the size of catalyst particles. Especially for noble metals, the atomically dispersed metals can achieve the highest utilization of metal atoms and reduce the material cost. For example, noble metals such as Pt, Pd, Ru, Rh and Ir are reported as superior heterogeneous catalysts in the petrochemical industry, medicine production, environmental protection, and new energy applications[58-61]. However, due to high costs and low natural abundances, It is still expensive to use noble metal NPs in many applications.

To address these issues, the downsizing of noble metals from nanoclusters to isolated single atoms is the most effective method to provide optimal active sites in corresponding catalysts to maximize metal atom efficiency and maintain necessary catalytic performances. Here, metal single-atom catalysts (M-SACs), a class of catalysts in which catalytically active individual and isolated metal atoms are anchored to supports, have emerged as a novel class of catalysts that can exhibit optimal metal utilization, with all metal atoms being exposed to reactants and available for catalytic reactions[42, 62]. Furthermore, the unique properties of M-SACs have attracted great attention from researchers due to distinct behaviors in comparison with metal-NPs in which extraordinary catalytic activity, selectivity, and stability for various reactions[63-65].

Since the first practical Pt-SAC(Pt1/FeOx) catalyst was reported by Zhao et al., significant progress has been made in this rapidly emerging field, with various supported M-SACs with different metals being designed and tested to exhibit excellent

catalytic performances in various chemical reactions[66]. For example, numbers of carbon supported M-SACs were reported with superior activity for oxidation reactions[4, 67]. Recently, Guan and co-workers reported a cobalt single-atom catalyst supported on nitrogen-doped graphene (denoted as CoNG) for the oxidation of alcohols[68]. The existence of a Co atomic sites was confirmed by an HAADF-STEM analysis. Notably, the coordination of N with Co helps to manage a higher number of cobalt species. The Co-NG catalyst revealed great performance for selective oxidation of numerous alcohols including 4-chlorobenzyl alcohol, 4-methyl-benzyl alcohol, and 4-methoxy-benzyl alcohol and could be recycled easily up to four cycles without a substantial loss of the catalytic activity/ selectivity[68].

Besides, the single atom catalysts were also developed for coupling reactions[69]. Cross-coupling reactions represent important chemical processes where various catalysts including noble metals are applied to achieve C−C, C−N, C−O, and C−S bond formations[70]. Recently, Pérez-Ramırez and co-workers reported the Pd atomic sites on exfoliated graphitic carbon nitride (Pd-ECN), which exhibited excellently high selectivity and wide-ranging functional group tolerance for Suzuki couplings and also outperformed flow reactions[71]. Additionally, Fe, Ni, Co, Zn and Pt based M-SACs have been reported with promising activity in ORR[72], CO_2RR[73], NRR[74] and NO_3RR[12]. For example, Zheng[75] reported a Ni-based SAC (denoted as Ni-NCB) by depositing Ni on low-cost N-doped carbon black and applied it for CO_2RR toward CO. Ni-NCB displayed an excellent performance for CO_2RR when tested in a traditional H cell under 0.55 V overpotential in a 0.5 M$KHCO_3$ aqueous electrolyte. The superior catalytic

performance was attributed to the high Ni mass loading, the maximum utilization efficiency of Ni atoms, and the gas diffusion layer[75]. In another study, atomically dispersed FeN_5 single-atom sites were embedded in N-doped graphene (denoted as FeN_5) and further used for electrocatalytic reduction of CO_2. FeN_5 exhibited a high FE toward CO at 97.0% under an overpotential of 0.35 V[76]. In addition to the CO_2RR, an Fe-based CS-SAC (denoted as FeSA-N-C) was synthesized by modulating polypyrene-iron coordination complexes, yielding atomically dispersed Fe atoms on N-doped graphene-like structures which obtained FE of NH_3 up to 56.55%, with an yield of 7.48 $mg/h/mg_{cat}$[77]. DFT calculation results suggested that FeSA-N-C can effectively boost the access of N_2 with a low energy barrier of 2.38 kJ/mol. The localized high concentration of N_2 around Fe sites can facilitate N_2 adsorption with a low binding Gibbs free energy of -0.28 eV[77]. Mo-based CS-SAC (denoted as SA-Mo/NPC) was also synthesized by anchoring Mo atoms on N-doped porous carbon. Due to the high density of MoNx active sites on hierarchically porous carbon frameworks, the catalysts obtained a promising activity in NRR[78].

Besides, the strong interaction of various metal atoms and the nitrate groups was investigated by Chen as shown in Figure 1.3a[79] The Cu atoms obtained the strongest adsorption energy comparing with other two metal atoms. Meanwhile the strong interaction between metal atoms and BN substrate was also studied through computational calculation[80]. The formation energy of M-BN sites and the distance between metal atoms and BN substrate were characterized as Figure 1.3b. The Cu atoms can be stabilized on the BN surface with moderate formation energy with the shortest

distance on the surface, which indicates the strongest interaction with the substrate. These conclusions make the $CuBN_x$ a promising catalyst for NRR and NO_3RR.

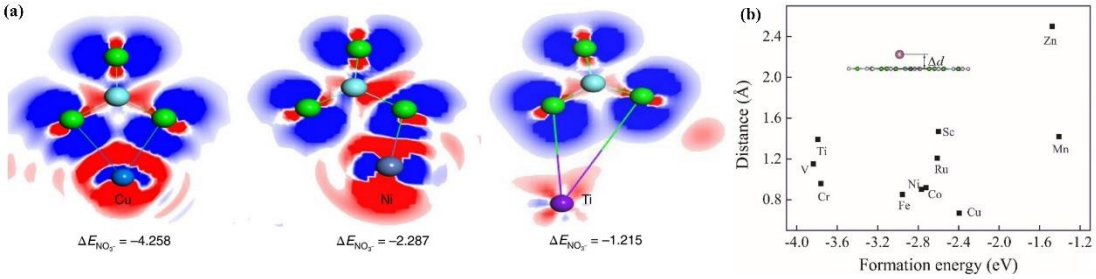

Figure 1.3 The promising $CuBN_x$ catalysts (a) the adsorption energy of NO_3^- species on metal atoms[79]; (b) the formation energy and bond distance of MBN_x[80].

However, due to the high mobility of metal atoms on the surface, it is still challenging to reliably synthesize M-SACs. Generally, the preparation techniques for these types of single-atom catalysts are organized into two fundamental classes: in situ preparation and post preparation. The former category includes various approaches such as chemical vapor deposition (CVD), atomic layer deposition (ALD), pyrolysis, solvothermal synthesis, and ball-milling (with the attention to prevent addition of impurities)[81]. Comparing with CVD and ALD which require expensive instruments and having difficulties of scaling up, pyrolysis is considered the most feasible synthesis method for M-SACs[82]. The precursors include polymers, MOFs, and many other organic compounds containing metal species. Among them, various polymers are the most widely used precursors to form carbon substrates for M-SACs by high-temperature pyrolysis because of the following reasons: (1) a variety of dopants, such as O, N, and S, can be precisely introduced into the framework of polymers, which lead to specific heteroatom dopants in the carbon substrates for metal ion adsorption;

(2) the structures of carbon substrates, such as pore size, surface area, and bulk geometry, can be easily controlled by the polymer structures, solvents, and pyrolysis conditions; (3) polymers can also create carbon substrates with distinct atomic arrangements, which facilitates the study of structure-activity relationships in CS-SACs[83]. For example, Zhao and coworkers[84] polymerized dicyandiamide and Ni(II) acetylacetonate to synthesize a Ni-based SAC (denoted as NiSA-N-CNT) supported on tubular carbon structures for CO_2RR, which has an ultrahigh Ni mass loading of 20.3 wt. %. Figure 1.3a shows that the single Ni atoms coordinate with four nearest N atoms. The ratio of the Ni precursor and dicyandiamide can significantly affect the morphology of the obtained samples. The formation of tubular substrates is ascribed to the stress-introduced rolling of Ni-containing graphitic carbon nitride layers under high temperatures and electron beam irradiation conditions. In another study, Cheng's group[85] polymerized hemin porcine (HP) with Fe(III) acetylacetonate to synthesize an Fe-based SAC supported on graphene-like 2 dimensional (2D) carbon nanosheets for fuel cells in an acidic electrolyte. The HP precursors are assembled into 2D carbon nanosheets, resulting in a high surface area. To increase the defect concentration in the substrate, the dual (S and N)-doped polymers have been designed and used for the Fe-based SAC synthesis. The dual-doped polymers can create more anchoring sites and optimize the interactions between carbon substrates and metal atoms, leading to outstanding catalytic performances. Thus, in this work, pyrolysis is used as a universal synthesis method to prepare M-SACs for electrocatalysis applications (NRR and NO_3RR) to mitigate the climate challenge and disturb the chemical industry for a more

sustainable development.

Figure 1.4 The synthesis strategies for M-SACs.

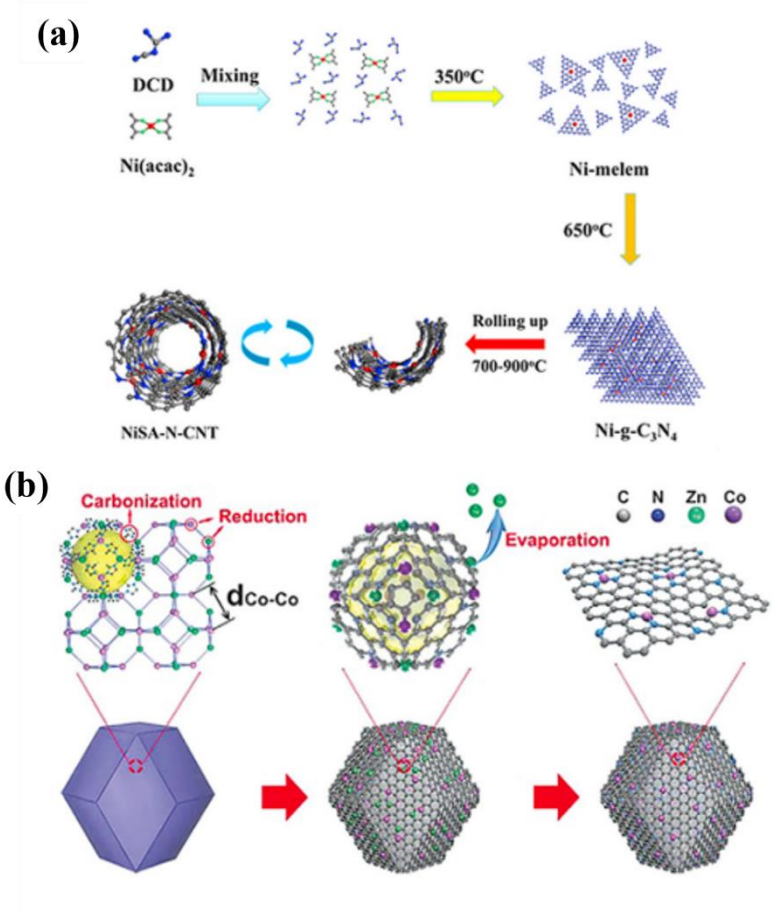

Figure 1.5 Schematic illustrations of the synthesis of pyrolysis method (a) NiSA-N-CNT[84]. The red and blue dots represent Ni and N atoms, respectively. (b) CoSA/N-C[85].

1.2 Objectives

The overall production of NH_3 from either NRR or NO_3RR pathways is still away from commercialization, as shown in the Table 1. The objective of this work is to develop a universal synthesis strategy for porous boron nitride supported transition metal single atom catalysts (MBN) for electrochemical reduction reaction of nitrogen (NRR) and nitrate (NO_3RR) to expand the production of ammonia and mitigate the climate challenge caused by the emission of CO_2. The transition metals were screened out to identify the most active catalyst both in NRR and $CuBN_x$ catalysts were thoroughly investigated in NO_3RR. Various characterization techniques were used to identify the chemical environment of the catalysts to further improve the catalytic performance. Finally, the oxygen plasma treatment was applied to tune the oxidation state of Cu and improve the activity.

Table 1.1 The NH_3 Productivity from NRR and NO_3RR

Catalysts	FE	NH_3 yield	Methods	Ref
Pd/C	8.2%	4.5μg/h/g_{Pd}	NRR	[86]
Fe_{SA}-N-C	56.55%	7.58 μg/h/g_{cat}	NRR	[77]
BNS	4.04%	13.22 μg/h/g_{cat}	NRR	[56]
B_4C	15.95%	26.57 μg/h/g_{cat}	NRR	[87]
Ru SAs/N-C	29.6%	120.9 μg/h/g_{cat}	NRR	[88]
CuNanosheets	99.7%	389.3 μg/h/g_{cat}	NO_3RR	[89]
Fe-MoS_2	90.2%	510 μg/h/g_{cat}	NO_3RR	[90]
Cu_2O	82.35	743 μg/h/g_{cat}	NO_3RR	[91]
$ZnCo_2O_4$	95.4	2100 μg/h/g_{cat}	NO_3RR	[92]
BCN-Cu	98.23	3358.74 μg/h/g_{cat}	NO_3RR	[93]

Note: ordered by the productivity.

CHAPTER 2

$CuBN_x$ CATALYSTS FOR NITROGEN REDUCTION REACTION

2.1 Introduction

Ammonia (NH_3), as a key feedstock for synthetic fertilizer as well as an energy carrier, is essential for human society, especially for supporting the increasing global population[94, 95]. Nitrogen (N_2), although abundant in the atmosphere is kinetically inert due to the strong NN triple bond (bond energy: 941 kJ mol^{-1}), especially considering the very high first bond cleavage energy of 410 kJ mol^{-1} [96, 97]. Therefore, the production of NH_3 by reacting N_2 with H_2 is energetically challenging. To date, the Haber–Bosch method, which is normally carried out under harsh conditions of high pressure (150–350 atm) and high temperature (350–550 °C), is still the most popular process for the industrial-scale production of ammonia[98, 99]. In this and the associated processes (e.g., to produce H_2 from fossil fuels), a large amount of energy is consumed, accompanied by the release of large quantities of carbon oxides[100]. Consequently, ammonia production consumes up to 1–3% of the global energy supply and contributes to the range of 1.6–3% of total CO_2 production, making this process non sustainable and not energy efficient[101, 102]. Therefore, the development of an efficient way to reduce N_2 to NH_3 under ambient conditions is of great importance and has attracted ongoing research interest.

Pioneering works applying various noble metal based N_2 reduction reaction (NRR) catalysts (e.g., Au, Pt, Ru, Ag) as well as several recent examples of transition

metals and non-metal catalysts have already demonstrated the extraordinary advantages of these heterogeneous electrocatalysts, although the overall efficiency remains unsatisfactory[103-105]. For example, noble metal-based electrocatalysts like Ru- and Au-based compounds are among the highest activity catalysts for ammonia synthesis[88, 106], while their scarcity and high costs make their large-scale application almost impossible. Therefore, transition metal-based electrocatalysts are regarded as promising catalysts for NRR on account of the π-back donation feature based on the availability of d-band electrons that enables the activation and cleavage of N_2 [107, 108]. Owing to the transition metal electronic structure, high reserves and low cost of Cu, Cu-based electrocatalysts have attracted broad interests and achieved significant progresses for efficient nitrogen reduction recently[103, 109]. Rational catalysts design strategies such as morphology engineering, defect introduction and component regulation play significant roles in optimizing the morphology and structure of catalysts to further increase the catalytic activity and active site densities for enhanced N_2 reduction response.

Meanwhile, as a substitute of carbon materials, boron nitride (BN) was investigated as both catalyst and support in various applications. Boron nitride (BN) nanomaterials, especially boron nitride nanotubes (BNNTs), have also emerged as potential candidates for heterogeneous catalysis because of BN's structural similarity to graphene[110].

To combine the superior activity of BN and metal atoms, we synthesized porous boron nitride supported transition metals catalysts (MBN_x) for NRR with a significant potential scale to simultaneously depress the hydrogen evolution reaction (HER)

activity and elevate the NRR activity and achieved a higher Faradaic efficiency and yield rate of NH_3 (118.3μg /h/g^2).

2.2 Experimental

In this section, BN_x supported transition metal single atom catalysts were prepared with different metal loading by pyrolysis method. The properties of the MBN_x catalysts were characterized by using XRD and NH_3 TPD. The use of MBN_x catalysts in NRR was conducted in a self-designed H-Cell to investigate the effect of metal loading and B/N ratio in BN subtract on their catalytic performance.

2.2.1 MBN_x synthesis

All the materials and chemicals were commercially available and were used without further purification. Preparation of BN_x was based on the reported synthesis of porous BN[111, 112]: The intermediates consisted of a mixture of urea and boric acid that the boric acid was first dissolved in 80mL of DI water. Then a certain amount of urea was added to the solution. The mixer was further dried at 75 ℃ for 20 hours. The molecular ratios of urea and boric acid are equal to 1:12, 1:24, and 1:36, respectively. These were selected as they enabled the production of porous BN while obtaining a good porosity and stability after high-temperature treatment. After drying the urea and boric acid, the mixture was heated at 600 ℃ for 4 hours with the protection of N_2 gas (30sccm).

Preparation of MBN_x: The intermediates consisted of a mixture of urea and boric acid dissolved in DI water with the same procedure of the synthesis of BN_x. Then a certain amount of metal precursor (metal acetylacetonate) was added into the solution

slowly with vigorous stirring. After drying, the mixture was heated at 600 ℃ for 4 hours with the protection of N_2 gas (30sccm). Then the sample was collected and grinded for the NO_3RR test.

2.2.2 MBN_x characterization

XRD: To get the crystal information, powder XRD patterns were recorded monochromatic Cu Kα radiation (λ = 1.5406 Å). XPS data was obtained from a Thermo Scientific ESCALAB 250Xi with a monochromic Al Kαradiation.

NH_3 TPD: NH_3 TPD was used to characterize the adsorption properties of the catalyst. It was carried out in the AutoChem 2920 automated characterization system (Micrometrics) equipped with a thermal conductivity detector (TCD). The thermal conductivity detector was used to measure NH_3 desorbed from the surface during TPD experiment. An ice water trap was used to remove moisture from the TPD effluent stream before the TCD. 100 mg of sample was generally loaded in a quartz U-tube. The TPD was performed after 2 hours drying in N_2 protection at 200 ℃. Then, 30mL/min of 10 vol.% NH_3/Ar was continuously flowing through the tube until the balance of the background. Then, the TPD experiment starts with heating from room temperature to 300 ℃ at a heating rate of 10 ℃/min and TCD signal was recorded by an online computer.

2.2.3 Catalyst test and products analysis

Electrocatalytic reduction of nitrate: A three-electrode sealed H-type cell was used in all electrochemical tests. The lading of catalysts was based on our previous methods[113]. Catalysts (50 mg) were dispersed in a solution of ethanol (0.3 mL), and 5 wt.% Nafion

solution (0.011 mL). After sonication for 4 min, a uniform ink-like dispersion was obtained. Next, 11 μL of the dispersion was dropped onto a polished glassy carbon electrode (GCE), and the resulting electrode was allowed to dry in air for half an hour. This catalyst/GCE served as the working electrode in subsequent electrochemical tests. An Ag/AgCl electrode and a Pt wire were used as the reference electrode and the counter electrode, respectively. The electrochemical nitrogen reduction was performed by chronoamperometry with the potential ranging between 0V and -1.3V for 1 hour to obtain the reduction efficiency and the distribution of products under various conditions.

Determination of ammonia: Ammonia-N was determined using Nessler's reagent as the color reagent[114, 115]. First, 0.3 mL of electrolyte was taken out from the electrolytic cell and diluted to 2.7 mL in the cuvette. Next, 0.2 mL potassium sodium tartrate solution (ρ=500 g/L) was added and mixed thoroughly, then 0.1 mL Nessler's reagent was added into the solution. The absorption intensity at a wavelength of 420 nm was recorded after sitting for 30 min. The concentration-absorbance curve was calibrated using a series of standard ammonium chloride solutions and the ammonium chloride crystal was dried at 75℃ overnight in advance.

Calculation of Faradaic Efficiency (FE) and NH_3 Yield Rate:

FE refers to the percentage of the electric charge used for NH_3 production compared to the total electric charge used during the NRR electrocatalysis process, which can be calculated by the following equation:

$$FE = C_{NH3}VNF/(17Q) \quad (2.1)$$

where C_{NH3} is the concentration of NH_3 (μg/mL), V is the volume of the

electrolyte (mL) and N is the number of electrons transferred for NH_3 generation, which equals 3. F refers to Faraday's constant (96485 C mol-1), Q is the total electric charge used for the working electrode.

The NH_3 yield rate means the yield of NH_3 of the catalyst over a certain reaction time. It was calculated using the following equation:

$$vNH_3 = C_{NH3}V/m_{cat}.\ t \quad (2.2)$$

Where t is the reduction time (min) and m_{cat}. is the loading mass of catalyst (mg). In our experiment, we assume that the Cu atoms in the electrocatalysts are the active site for electrochemical N_2 reaction.

2.3 Results and Discussion

2.3.1 Structural characterization

The nanocrystalline nature of the MBN_x was studied by X-ray diffraction (XRD), as shown in Figure 2.1. The XRD results of other MBN samples are shown in Figure 2.1a without any characteristic peaks detected. Then $CuBN_x$ catalysts were selected to study the metal loading effect due to a better activity than other M/BN_x catalysts. The XRD proved that when the metal loading is lower than 1wt%, there are no characteristic peaks detected due to the well dispersion of Cu on the surface. On the contrary, there are two characteristic peaks detected for $CuBN_x$-2wt and $CuBN_x$-3wt samples that the peaks at 43° and 50° can be assigned to the (111) and (200) planes of the cubic phase of Cu, respectively.

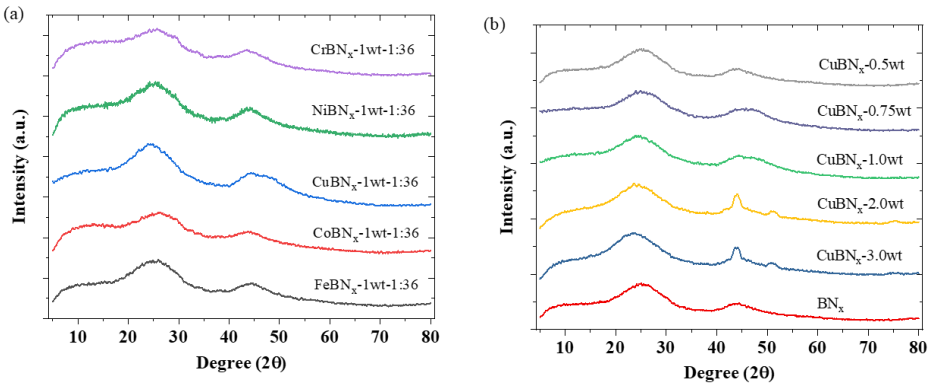

Figure 2.1 XRD characterization of MBN_x samples.

2.3.2 Catalytic performance

At first, different metals were investigated to study the metal effect on the reaction performance as shown in Figure 2.1a. Porous BN supported Fe, Co, Ni and Cr were prepared with the same experimental procedure. The XRD (Figure 2.1b) implies that with 1wt% loading of the metal, metal atoms were highly dispersed on the surface and serving as the active sites in NRR. However, the performance of different metals is different, which is due to the intrinsic properties of metal atoms. NH_3-TPD (temperature programmed desorption) was conducted on MBN_x catalysts to explain the performance difference. As shown in Figure 2.2b, the $CuBN_x$ sample provides the highest content of NH_3 desorption which indicates the highest content of Lewis's acidity sites of M-BN_X sites than other metals, which resulted in a better NRR performance of M-BN_X. The Cr and Ni provided the lowest content of acid sites for ammonia desorption. Pei's recent work also reported that the transition metal doped BN_X sites has a moderate adsorption of different intermediates in the NRR[80].

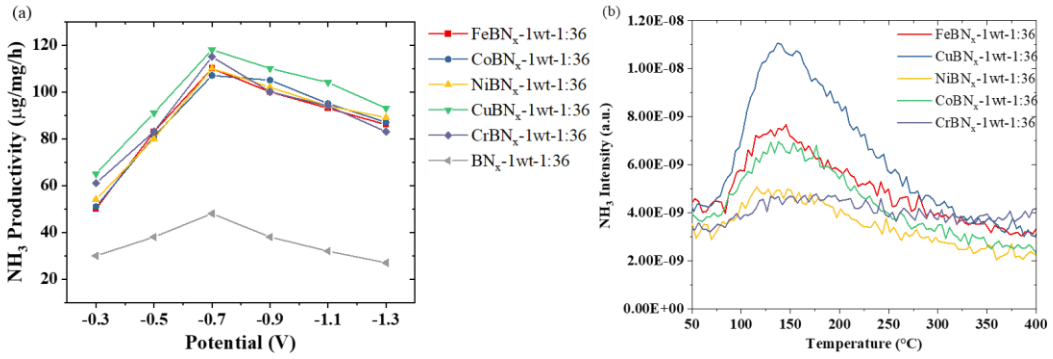

Figure 2.2 The NRR performance of MBN_X and the TPD results (a) NRR performance; (b) the TPD results.

Then, the $CuBN_x$ catalysts were studied thoroughly to optimize the reaction performance and to reveal the origin of the promising activity. The electrochemical NRR measurements were performed under atmospheric pressure and ambient temperature. To evaluate the electrocatalytic activity of $CuBN_x$ in acid electrolyte, linear sweep voltammetry (LSV) curves of $CuBN_x$ were first collected in both N_2-saturated and Ar-saturated 0.05M H_2SO_4, respectively (Figure 2.3 a).

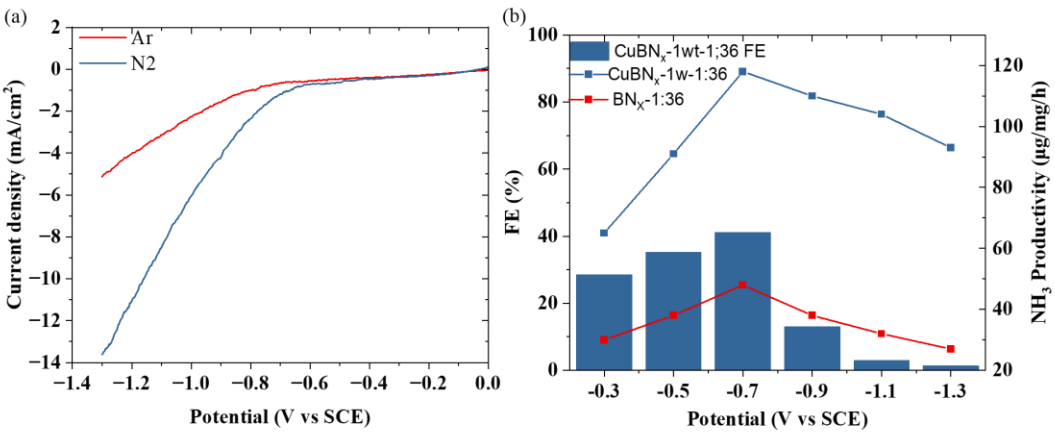

Figure 2.3 NRR electrochemical performance of $CuBN_x$ (a) LSV curves in N_2-saturated and Ar-saturated 0.05M H_2SO_4 electrolytes; (b) NH_3 yield rate and FE at different potentials in 0.05M H_2SO_4.

An apparent current density gap can be observed in the potential window from -0.3 to -1.3 V, indicating that the electrochemical reduction of N_2 has occurred. After that, chronoamperometry tests were conducted on $CuBN_x$ catalyst and on BN_x as a comparison at different applied potentials for half an hour (from -0.3 to -1.3V vs SCE). The products of NH_3 were immediately detected after electrolysis and quantified by Nessler reagent. The ultraviolet-visible (UV-vis) absorption spectra of the electrolyte colored with Nessler reagent demonstrates that NH_3 is generated by N_2 electroreduction. The calibration of colored electrolyte is shown in Figure 2.4a and b, and the NH_3 production of $CuBN_x$-1wt sample and the effect of substrate are plotted in Figure 2.3b. The highest NH_3 production rate of $CuBN_x$-1wt sample and the substrate were obtained as 118.3 $\mu g/h/mg_{cat}$ and 48 $\mu g/h/mg_{cat}$, respectively. Such high NRR activity of $CuBN_x$ sample compares favorably with previous reported NRR electrocatalysis (Table 1.1). The porous BN obtained a relatively high NRR activity, which may be due to the formation of isolated boron active sites. Sun and coworkers also published a computational work and proved that the isolated B atoms are active sites for NRR. The sp^3 hybrid orbital of the boron atom can form B-to-N π-back bonding. This results in the population of the N−N π* orbital and the concomitant decrease of the N−N bond order[116]. An experimental work also mentioned that the boron atoms served as the Lewis acid sites for the reaction. The B-enriched BCN nano mesh presented outstanding NRR performance with an ammonia yield of 41.9 $\mu g/h/g_{cat}$ and FE of 9.87 %, together with an excellent stability[117].

In addition, the loading of Cu on porous BN_x introduced more active sites for

NRR, which results in over 100% improvement of the activity from porous boron nitride. However, a further negative shift of the applied potentials leads to a dramatic decreasing of NH_3 yield rate due to enhance of HER activity[118].

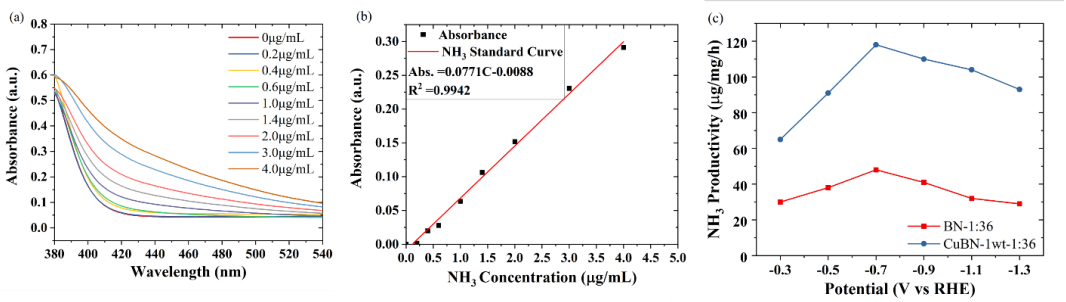

Figure 2.4 UV-vis calibration curves and the determined NH_3 productivity.

For further understanding of the interaction between boron atoms and Cu atoms, the loading of Cu and boron was studied with different Cu loading and B/N ratio from 1:12 to 1:48 (NRR tested at -0.7V vs SCE). The mountain-shape of the NH_3 productivity confirmed that 1:36 of B/N ratio is the optimized ratio in the reaction. Further BET study of the samples implied that the B/N ratio is critical to the surface area of the sample which is a critical parameter to form isolated boron atoms on the surface. If the boron concentration is too high, for example, the $CuBN_x$-1:12 sample has lower surface area than $CuBN_x$-1:24 and $CuBN_x$-1:36 sample, and the boron bonded together which resulted in a lower activity. However, when the B/N ratio is higher than 1:48, more Cu active sites were covered by undecomposed nitrogen precursor on the surface which resulted in the decreasing of the activity. The full comparison of $CuBN_x$ and BN with different B/N ratio is shown in Figure 2.5 b, which clearly indicates the optimized performance of $CuBN_x$ sample with B/N ratio of 1:36. In addition, the

different usage of urea in the synthesis process of $CuBN_x$, it is difficult to determine the characterize the structure change of BN subtract from XRD, thus the effect of B/N ratio will be further studied in the future.

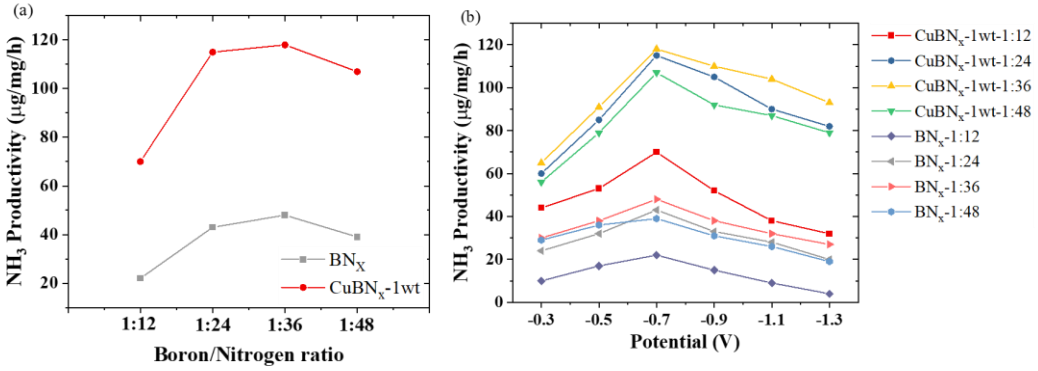

Figure 2.5 The B/N ratio effect on NRR performance.

Table 2.1 The Surface Area of $CuBN_x$-1wt Samples with Different B/N Ratio.

B/N ratio	BET surface area (m^2/g)
1:12	20.17
1:24	32.58
1:36	43.66
1:48	55.8

After the investigation of B/N ratio, the Cu loading effect was investigated with different Cu loading with fixed B/N ratio of 1:36. The catalytic performance of NRR was conducted at different potentials as shown in Figure 2.6. The $CuBN_x$-1wt-1:36 obtained the highest performance of 118.3 $\mu g/h/g_{cat}$. The similar changing pattern of the NH_3 productivity of $CuBN_x$ sample with the Cu loading less than 1wt% indicating

linear relationship of NH_3 productivity and Cu loading. However, with Cu loading higher than 2wt%, the decreasing of NH_3 productivity results from the formation of large Cu particles. The XRD results also confirmed the formation of metallic Cu of $CuBN_x$ with 2 and 3 wt.% of Cu loading. As shown in Figure 2.1b, no peak of metallic Cu was detected from XRD for BN and $CuBN_x$ with Cu loading less than 1wt%. On the contrary, two characteristic peaks for metallic Cu were confirmed form XRD[119].

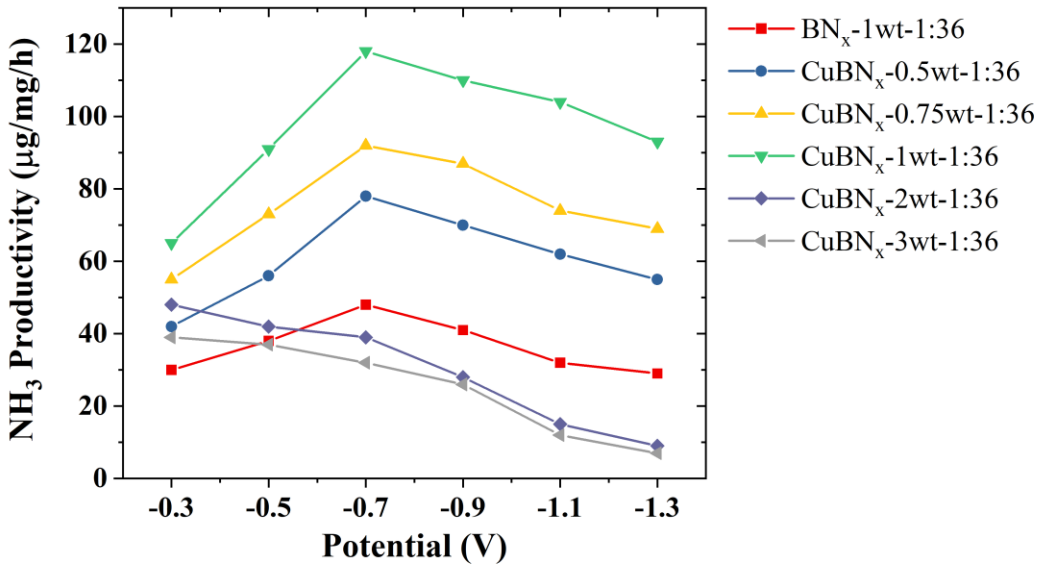

Figure 2.6 The NRR performance of $CuBN_x$ samples with different metal loading.

2.4 Summary

In this section, pyrolysis method was developed for the synthesis of MBN_x catalysts for NRR with promising activity. Various transition metals were screened out in the reaction and the $CuBN_x$ catalyst obtains the highest activity in comparison with Fe, Co, Ni and Cr. The NH_3-TPD results proved the higher content of Lewis acid sites of Cu BN than other metal catalysts. Thus, the higher reaction rate of $CuBN_x$ in NRR is origin from the intrinsic property of Cu. Besides the different metals, the metal loading effect

of Cu and the B/N ratio were also studied to investigate the role of Cu and B atoms. The NRR performance was also successfully optimized that the B/N ratio of 1:36 is considered the optimized synthesis formula with high surface area and no undecomposed groups blocking the active sites. The $CuBN_x$-1wt-1:36 obtained the highest NH_3 productivity of 118.3 μg/h/mg_{cat}. However, productivity should be further improved in the future. And it is still too early to confirm the formation of single atom sites on the surface due to the detection limitation of XRD. Thus, the XAS was used in the future to further investigate the chemical environment of metal atoms on the surface.

CHAPTER 3

$CuBN_x$ CATALYST FOR NITRATE REDUCTION REACTION

3.1 Introduction

Electrochemical nitrogen reduction (NRR) to synthesize NH_3 has been reported to operate under the room temperature and pressure but suffers the breaking of the triple bond of nitrogen and nitrogen with low Faraday efficiencies[120]. Besides, the low solubility of N_2 in aqueous solution is another limitation of the NRR[121]. Therefore, researchers are constantly looking for efficient and alternative NH_3 synthesis methods to replace traditional methods. From the perspective of economy and environmental protection, NO_3^- reduction reaction to synthesize NH_3 (NO_3RR)is an ideal choice[122, 123].

NO_3RR powered by renewable electricity is considered as a promising way for NO_3^- remediation because it can directly convert NO_3^- into NH_3 without waste generation[124]. More importantly, nitrate directly threatens human health by damaging the human endocrine system in the drinking water. To minimize the adverse health impacts of nitrate, the World Health Organization (WHO) has set a recommended maximum contamination level of 50mg/L NO_3^- in drinking water[125]. Thus, NO3RR is also considered a potential process for drinking water treatment to meet the WHO standards[126].

In recent years, NO_3RR is attracting more attention due to mentioned advantages. However, the overall activity of current catalysts is still away from real application. Among these developed catalysts, transition metal catalysts have attracted

much attention in the field of NO_3RR due to their advantages of high activity, abundant reserves, and cheap price[127, 128]. Copper-based catalysts are one of the metals with high catalytic activity for selective nitrate reduction to NH_3[129]. The copper-based catalysts with a special electronic structure exhibit the highest activity and selectivity in single-component metal catalysts for electrochemical NO_3RR. For example, copper nanosheets prepared by Kang et al. have an exposed copper (111) crystal plane and can effectively inhibit HER and significantly improve the rate-determining step. The formation rate of NH_3 from nitrate reduction is more than two orders of magnitude higher than that of electrochemical reduction of nitrogen[130]. Wang et al. combined copper with 3,4,5,9-perylenetetracarboxylic dianhydride to obtain a novel catalyst. The unique electronic configuration of copper on the surface is conducive to the adsorption and electron transfer of nitrate ions, which can effectively inhibit HER and promote the NO3RR processes[79]. However, the overall performance of NO3RR on Cu based catalyst is not desirable. Recently, metal based single atom catalyst, especially Cu base SACs exhibited promising catalytic performance in NO_3RR[25, 131]. Minimizing Cu to the nanoscale, even single-atom level, can overcome the limitations of bulk material. For instance, Fu et al. prepared nanoscale Cu nanosheets by a solution-phase synthesis method, which achieved a yield of 390.1 μg/h/mg_{cat} and 99.7% FE of ammonia at a low overpotential of −0.15 V versus reversible hydrogen electrode (RHE)[130]. Zhu et al. synthesized single-atom Cu−N−C catalysts by immobilizing Cu single atoms on nitrogenated carbon nanosheets, which exhibited a superior NO_3^- conversion of 97.3%[132]. However, more effort should be made to further improve the performance of

Cu single atom catalyst. In this section, the Cu single atom catalyst was synthesized on porous BN_x via pyrolysis method. The NO_3RR activity was investigated with different B/N ratio and Cu loading. Characterization from XRD and XAS implied the formation of Cu single atomic sites on the surface as the active sites.

3.2 Experimental

In this section, BN_x supported copper single atom catalysts were prepared with different metal loading by pyrolysis method. The properties of the $CuBN_x$ catalysts were examined by using Brunauer-Emmett-Teller (BET), temperature-programmed reduction (TPR), X-ray diffraction (XRD), and X-ray absorption spectra (XANES). The catalytic performance of $CuBN_x$ was tested in a self-designed H-Cell to investigate the effect of Cu loading and B/N ratio.

3.2.1 $CuBN_x$ synthesis

All the materials and chemicals were commercially available and were used without further purification. Preparation of BN_x: The intermediates consisted of a mixture of urea and boric acid that the boric acid was first dissolved in 80mL of DI water. Then a certain amount of urea was added to the solution. The mixer was further dried at 75 ℃ for 20 hours. The molecular ratios of urea and boric acid are equal to 1:12, 1:24, 1:36, and 1:48, respectively. These were selected as they enabled the production of porous BN while obtaining a good porosity and stability after high-temperature treatment. After drying the urea and boric acid, the mixture was heated at 600 ℃ for 4 hours with the protection of N_2 gas (30sccm).

Preparation of $CuBN_x$: The intermediates consisted of a mixture of urea and boric acid dissolved in DI water with the same procedure of the synthesis of BN_x. Then a certain amount of Cu precursor (Copper acetylacetonate) was added into the solution slowly with vigorous stirring. After drying, the mixture was heated at 600 ℃ for 4 hours with the protection of N_2 gas (30sccm). Then the sample was collected and grinded for the NO_3RR test.

Preparation of Cu/Al_2O_3 (0.5 wt% is used to make sure the atomic dispersion of Cu). Certain amount of Al_2O_3 was pre-calcined at 500 ℃ to remove all absorbed molecules. Then the $Cu(NO_3)_2$ were weighted and dissolved in water to form Cu solutions with low concentration. Then the Cu atoms were loaded on Al_2O_3 with dry impregnation method. After drying in the oven for 10 hours, the samples were calcined in open air at 200 ℃ for 2 hours. The samples were tested without further treatment.

3.2.2 $CuBN_x$ characterization

BET surface area measurement: The specific surface areas were calculated by Brunauer-Emmett-Teller (BET) method on Micromeritics AutoChem 2920 automated characterization system (Micromeritics). Adsorption at liquid nitrogen temperature was performed using a 30% N_2/He stream, and the desorption area obtained after rapid heating was compared with the area of a calibrated volume. The amount of desorbed nitrogen molecules was used for the surface calculation.

TPR: TPR was used to reduce CuO_X species of the catalyst. It was carried out in the AutoChem 2920 automated characterization system (Micrometrics) equipped with a thermal conductivity detector (TCD). The thermal conductivity detector was

used to measure H_2 consumption during TPR experiment. An ice water trap was used to remove moisture from the TPR effluent stream before the TCD. 100 mg of sample was generally loaded in a quartz U-tube. The TPR was performed using 30mL/min of 10 vol.%H_2/Ar from room temperature to 600 ℃ at a heating rate of 10 ℃/min and TCD signal was recorded by an online computer.

NH_3 TPD: NH_3 TPD was used to characterize the adsorption properties of the catalyst. It was carried out in the AutoChem 2920 automated characterization system (Micrometrics) equipped with a thermal conductivity detector (TCD). The thermal conductivity detector was used to measure NH_3 desorbed from the surface during TPD experiment. An ice water trap was used to remove moisture from the TPD effluent stream before the TCD. 100 mg of sample was generally loaded in a quartz U-tube. The TPD was performed after 2 hours drying in N_2 protection at 200 ℃. Then, 30mL/min of 10 vol.% NH_3/Ar was continuously flowing through the tube until the balance of the background. Then, the TPD experiment starts with heating from room temperature to 300 ℃ at a heating rate of 10 ℃/min and TCD signal was recorded by an online computer.

XRD: In order to get the crystal information, powder XRD patterns were recorded monochromatic Cu Kα radiation (λ = 1.5406 Å). XPS data was obtained from a Thermo Scientific ESCALAB 250Xi with a monochromic Al Kαradiation.

XAS: XAS data were processed with Demeter (v.0.9.26). Using Athena software in Demeter, XAS spectral was performed with normalization using a cubic spline function that was used to fit the background above the absorption edge. 2 Then,

the data was transformed to the normalized EXAFS function, χ(E), in energy space to χ(k), where k is the photoelectron wave vector. χ(k) was multiplied by k2 to amplify the EXAFS oscillations in the mid-k region for assessing the interatomic interaction of Cu atoms. To differentiate the EXAFS oscillation from different coordination shells, Fourier transformation (from k space to R space) of the k2 −weighted χ(k) with a k range of 3 − 11.5 Å−1 for the Cu K−edge was conducted. Subsequently, EXAFS data recorded in R space was fitted using Artemis software in Demeter with the FEFF6 program. The Cu first shell was fitted at an R range of 1.6 − 3.2 Å. The phase and amplitude functions of Cu−O and Cu−Cu were calculated with FEFF. A S0 value of 0.80 for Cu was determined from Cu foil, which was then applied to the Cu K−edge EXAFS fittings of the samples. From these standard EXAFS fitting practices, structural parameters of Cu samples were calculated, including coordination number (CN), bond distance (R), inner potential shift (ΔE), and Debye-Waller factor (σ2).

3.2.3 Catalyst test and product analysis

Electrocatalytic reduction of nitrate: A three-electrode sealed H-type cell was used in all electrochemical tests. Catalysts (50 mg) were dispersed in a solution of ethanol (0.3 mL), and 5 wt.% Nafion solution (0.011 mL). After sonication for 4 min, a uniform ink-like dispersion was obtained. Next, 12 μL of the dispersion was dropped onto a polished glassy carbon electrode (GCE), and the resulting electrode was allowed to dry in air for half an hour. This catalyst/GCE served as the working electrode in subsequent electrochemical tests. An Ag/AgCl electrode and a Pt wire were used as the reference electrode and the counter electrode, respectively. The electrochemical nitrate reduction

was performed by chronoamperometry with the potential ranging between 0V and -1.3V to obtain the reduction efficiency and the distribution of products under various conditions.

Determination of nitrite: Nitrite-N was determined using Griess reagent as the color reagent. First, mix equal volumes of N-(1-naphthyl) ethylenediamine (Component A) and sulfamic acid (Component B) to form the Griess Reagent. Prepare sufficient reagent for immediate experiments only (100 μL per spectrophotometer cuvette). Next, 0.3mL was taken out from the electrolytic cell and diluted to 2.9mL in the cuvette followed by mixing 0.1 mL of prepared Gress's Reagent. Then, incubate the mixture for 30 minutes at room temperature. The absorption intensity at a wavelength of 548 nm was recorded for further determination. The concentration-absorbance curve was calibrated using the standard nitrite-containing solution provided by the manufacturer.

Determination of ammonia: Ammonia-N was determined using Nessler's reagent as the color reagent. First, 0.3 mL of electrolyte was taken out from the electrolytic cell and diluted to 2.7 mL in the cuvette. Next, 0.2 mL potassium sodium tartrate solution (ρ=500 g/L) was added and mixed thoroughly, then 0.1 mL Nessler's reagent was added into the solution. The absorption intensity at a wavelength of 420 nm was recorded after sitting for 30 min. The concentration-absorbance curve was calibrated using a series of standard ammonium chloride solutions and the ammonium chloride crystal was dried at 75℃ overnight in advance.

Determination of nitrate: Nitrate-N was determined using the Nitrate kit from

HACH company without any further treatment. First, a certain amount of electrolyte was taken out from the electrolytic cell and diluted 40 times. Then, 0.2mL of the diluted electrolyte solution was added to the sample container provided with the nitrate kits. Next, 1mL of solution A was added to the sample container and shaken for 2 seconds. After waiting for 15 minutes, the absorbance was detected at 345 nm. The concentration-absorbance curves were calibrated using a series of standard sodium nitrate solutions. The sodium nitrate was dried at 75℃ overnight in advance.

The NO_3^-conversion can be calculated by the equation as follows:

$$NO_3^-\text{conversion} = \frac{\Delta c_{NO_3^-}}{c_0} \times 100\% \quad (3.1)$$

The initial concentration of NO_3^- is marked as c_0 and converted from molar concentration, the concentration of NO_3^- after the reaction is marked as $c_{NO_3^-}$ (μg/mL).

The concentration of NH_3-N and NO_2^--N after the reaction are marked as c_{NH_3} and $c_{NO_2^-}$, respectively. The selectivity of NH_3 can be calculated by the equation as follows:

$$NH_3\ \text{selectivity} = \frac{c_{NH_3}}{c_{NH_3} + c_{NO2-}} \times 100\% \quad (3.2)$$

The Faradaic efficiency of NH_3 can be calculated by the equation as follows:

$$FE_{NH_3} = \frac{n \cdot F \cdot c_{NH_3} \cdot V}{M_{NH_3} \cdot Q} \times 100\% \quad (3.3)$$

n represents the number of electrons transferred from nitrate to ammonia, here it is 8. V represents the volume of electrolyte (mL). In our electrochemical test, the left cell contains 50mL electrolyte, so V here is 50mL. M_{NH_3} represents the relative molecular mass of NH_3 (17g/mol). Q represents the total charge transferred in the entire reaction.

F is the Faradaic constant, which is 96485 C/mol. Therefore, the Faradaic efficiency of NH_3 can be calculated by the equation as follows.

3.3 Results and Discussion

3.3.1 Structural characterization

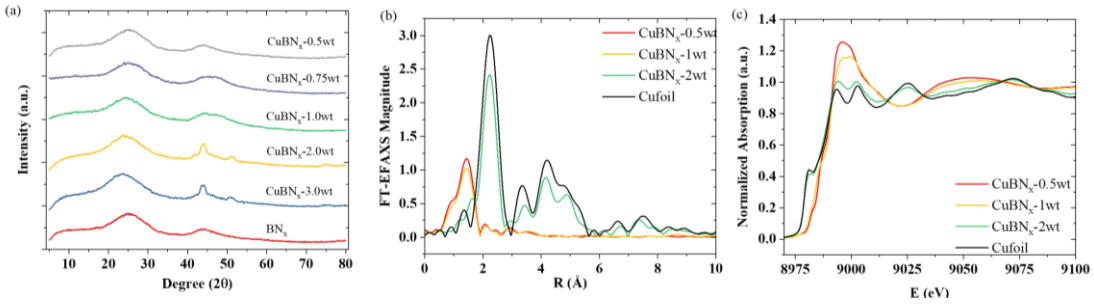

Figure 3.1 XRD and XAS characterization of $CuBN_x$ samples. (a) XRD spectra. (b) K3-weighted χ(k) function of EXAFS spectra. (c) Cu K-edge XANES spectra.

The nanocrystalline natures of the $CuBN_x$ and BN were studied by X-ray diffraction (XRD), as shown in Figure 3.1a. The $CuBN_x$-2wt and $CuBN_x$-3wt were characterized with two characteristic peaks of metallic Cu at 44.2 and 51.2 °, assigned to the (111), (200) planes of the face-centered cubic phase of Cu, respectively. The $CuBN_x$ with Cu loading less than 1wt% does not exhibit any Cu diffraction signals, because of the insensitivity of XRD toward the presence of single atoms.

The chemical environment of Cu atoms has been determined by X-ray absorption spectra (XAS) at the Cu K-edge. The near-edge spectra (Figure 3.1c) show features at 8981 (A), 8986 (B), 8993 (C), and 9002 eV (D), where the weak pre-edge peak A arising from the dipole-forbidden 1s → 3d transition can be employed to

fingerprint the presence of Cu^{2+} with a d9 electronic configuration[133], and the peak C is attributed to the 1s → 4p (continuum) electron transition of Cu^{2+} with the ligand effect on the transition rising as peak B[134], while peak D refers to the multiple scattering[135]. Furthermore, by comparing $CuBN_x$-0.5wt and $CuBN_x$-1wt samples with $CuBN_x$-2wt sample and the Cu foil, the higher oxidation phase of Cu in $CuBN_x$-0.5wt and $CuBN_x$-1wt samples is confirmed. The higher oxidation state of Cu species are preferred in the NO_3RR reaction which was also reported by other groups[136].

The local coordination structure of $CuBN_x$, X-ray absorption fine structure (XAFS) was further investigated with Cu foil as references, as shown in Figure 3.1b. The Fourier-transformed extended X-ray absorption fine structure (FT-EXAFS) spectrum of $CuBN_x$ samples shows a peak at 1.41 Å, which can be assigned to interaction between Cu and BN_x[137-139]. Such results imply that the isolated Cu atoms are well-dispersed on the porous support. As for $CuBN_x$-2wt, a main Cu−Cu characteristic peak can be detected at 2.20 Å, confirming the expected Cu clustering in the sample which is consistent with XRD results[133, 134]. On the contrary, there is no Cu-Cu bonding detected from $CuBN_x$-1wt and $CuBN_x$-0.5wt samples, which implies the isolation of Cu atoms and the formation of Cu single atom sites.

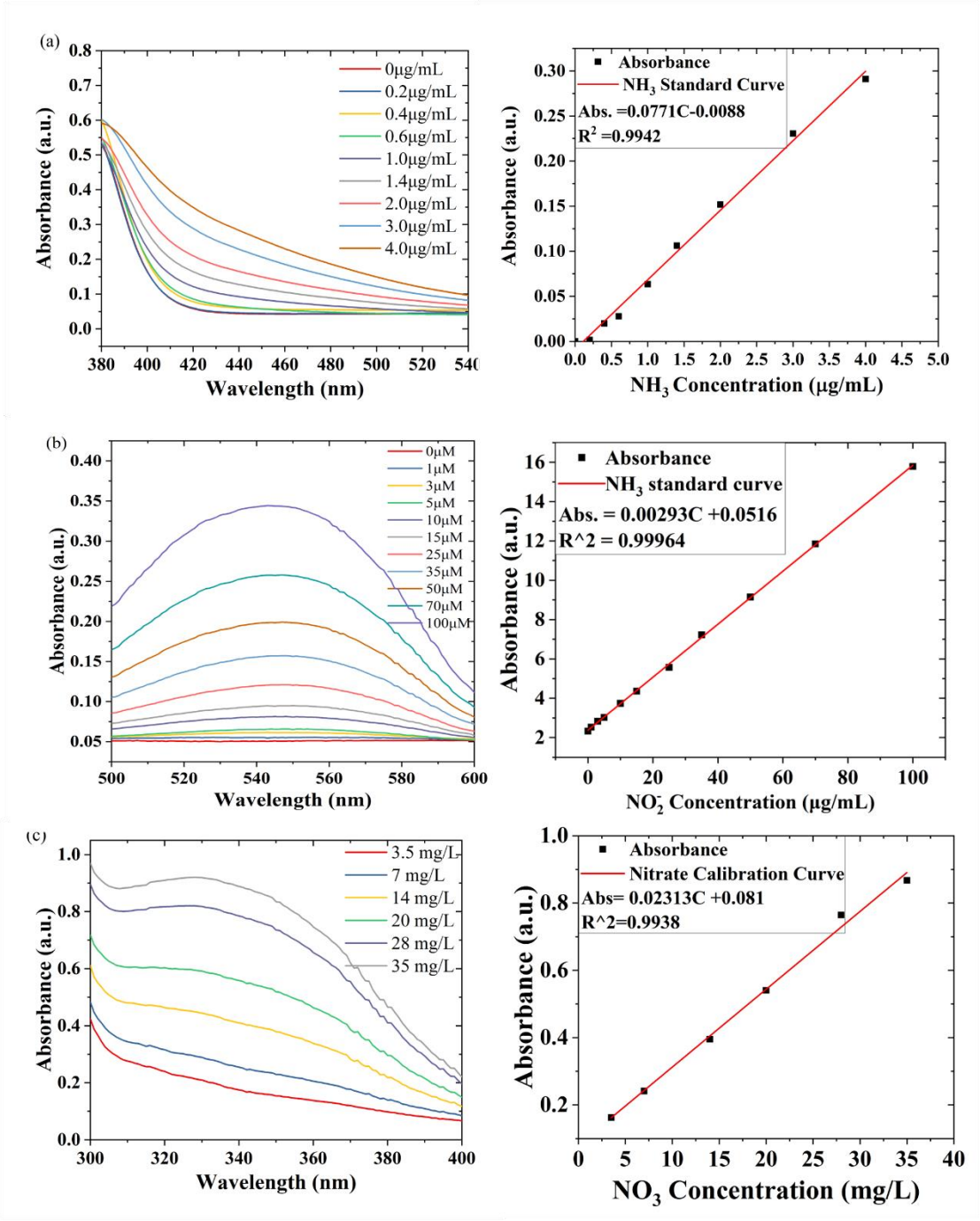

Figure 3.2 Calibration curve of products quantification (a) NH_3, (b)NO_2^- and (c) NO_3^-.

3.3.2 Catalytic performance

The NO_3RR activity of the catalysts was tested in a two-compartment H-cell system. The concentration of NO_3^-, NH_3 and NO_2^- were determined via the UV-vis spectrophotometry. The calibration curves are shown in Figure 3.2. To evaluate the catalytic performance of $CuBN_x$ samples and determine origin of the activity, the electrochemical performance of $CuBN_x$-1wt-1:36 and porous-BN_x were examined and compared. As shown in Figure 3.3a, the doping of Cu atoms on BN_x increased the NH_3 productivity dramatically (from 200 to 3190 ug/h/mg_{cat} at -0.7V vs SCE). Meanwhile, the current due to the transportation of electrons resulting in higher current with lower potentials applied as shown in Figure 3.3b. However, the productivity of NH_3 starts decreasing significantly, with the increasing productivity of NO_2^- as shown in Figure 3.3c, indicating that NO_2^- is an intermediate product during nitrate electroreduction. With higher potential applied on the working electrode, higher productivity of NO_2^- and controversially, lower productivity of NH_3 were obtained which implied the rate limiting step of reduction of NO_2^- at high potential window[136]. Besides, the FE of NH_3 was also calculated to investigate the competing reaction. As shown in Figure 3.3d, the FE and selectivity of NH_3 keep decreasing with higher potential applied, which is due to the side reaction of HER becoming the dominate reaction at high potential range[132].

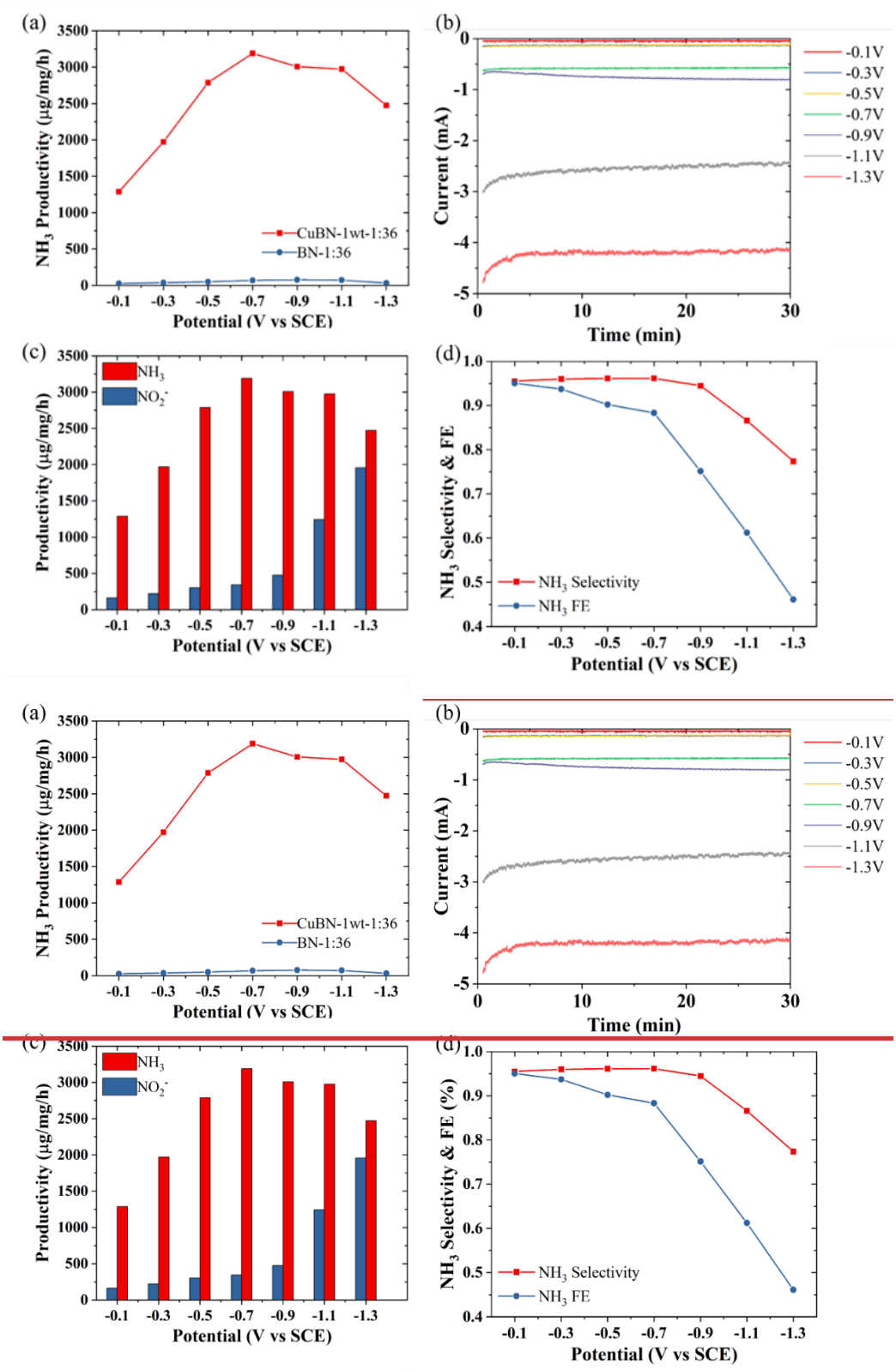

Figure 3.3 The catalytic performance of $CuBN_x$-1wt-1:36 sample (a) improvement of NO_3RR performance for $CuBN_x$-1wt-1:36; (b) Current collected at different potentials; (c) productivity of NH_3 and NO_2^- at different potentials applied; (d) the calculated FE and NH_3 selectivity.

To further investigate the origin of the activity and optimize the catalytic performance, the Cu loading effect, the BN ratio effect and the NO_3^- concentration effect was investigated. As shown in Figure 3.4a, with higher loading of Cu (from 0.5wt% to 1.0 wt%), the productivity of NH_3 increases from 1700 to 3200 μg/h/mg_{cat}, which is due to the higher content of Cu single atom sites on the surface. However, with higher loading of Cu, from 1wt% to 3wt%, the activity decreased significantly. The deactivation of high loading Cu samples was due to the formation of metallic Cu which was confirmed from XRD results. Other groups also reported the activity of single atomic transition metal catalysts in NO_3RR, NRR and CO_2RR[129, 132]. Besides, H_2-TPR results of $CuBN_x$ samples also indicate the increase of Cu active sites on the surface for the sample Cu loading from 0.5 to 1.0 wt.% and the decrease of Cu active sites for the samples with Cu loading from 1.0 to 3.0 wt.% The Cu loading also affects the surface area which is another important property as catalysts. With higher loading, especially from 1wt% to 3 wt.%, the surface area of the catalysts decreased from 50.21 to 12.58 m^2/g as shown in Table 3.1. Thus, the formation of Cu single atom sites and the accessibility of the single atom sites are critical to the NO_3RR.

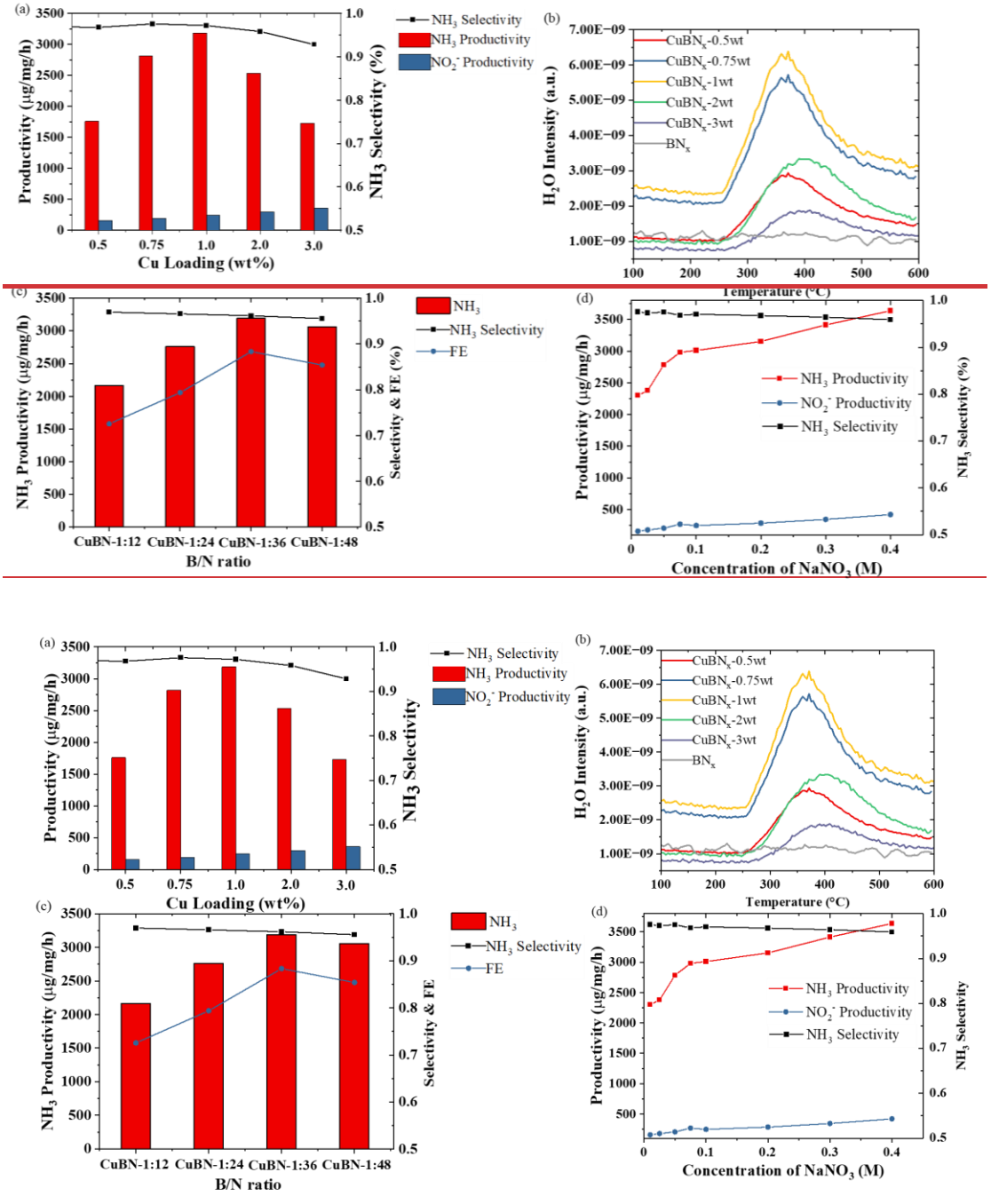

Figure 3.4 The effect of Cu loading, B/N ratio and $NaNO_3$ concentration on NO_3RR catalytic performance (a) the Cu loading effect on the NO_3RR catalytic performance; (b) temperature programmed reduction of $CuBN_x$ sample with different Cu loading; (c) the B/N ratio effect on the NO_3RR catalytic performance; (d) the $NaNO_3$ concentration effect on the NO_3RR catalytic performance.

To study the function of boron atoms, the B/N ratio was investigated as well. As shown in Figure 3.4c, the NH_3 productivity initially increased from 2200 to 3200

$\mu g/h/mg_{cat}$ from B/N ratio of 1:12 to 1:36 then decreased to 2800 $\mu g/h/mg_{cat}$ with B/N ratio of 1:48. The decrease of the catalytic performance when the B/N ratio increased from 1:36 to 1:48 was due to the poor pyrolysis process for the urea.

To further improve the production of NH_3, the concentration of NO_3^- in the electrolyte was increased. However, the productivity only improved about 20% in the electrolyte of 0.4M $NaNO_3$, which indicates that the catalytic performance is the rate limiting steps. Future efforts should keep focusing on the development of high activity catalysts, as shown in Figure 3.4 d.

Thus, it is concluded that when the content of boron atoms decreased by decreasing the usage of boron precursor in the synthesis process (B/N ratio from 1:12 to 1;36), a more porous structure with higher surface area is formed which provides isolated boron atoms as the active sites in the reaction which is preferred for the adsorption of N atoms[53, 80, 116]. On the other hand, when the boron concentration was further diluted to the ratio of 1:48, the performance decreased due to lower content of boron sites.

Besides, based on the recent literature, the metal single atomic sites were considered as the active sites for adsorption of NO_3^- in the reaction by acting as the week Lewis's acidity sites[140, 141]. To investigate the effect of Lewis's acidity, we compared the $CuBN_x$ with $CuAl_2O_3$ samples. The NH_3-TPD experiments were conducted to characterize the acidity of $CuBN_x$. As shown in Figure 3.5a $CuBN_x$ exhibited a week adsorption of NH_3 at 150°C, which is due to the week acidity of Cu-B bonding. The Cu/Al_2O_3 samples were tested as a reference which obtain two

characteristic desorption peaks of NH_3 at 150°C and 400°C for week adsorption of NH_3 and strong adsorption of NH_3, respectively. There is only limited NH_3 production from Cu/Al_2O_3, even though the samples have abundant Lewis's acid sites. It is clear that Lewis's acid sites are not the dominant contribution to NH_3 production. The interaction between Cu and BN_x plays an important role in the reaction.

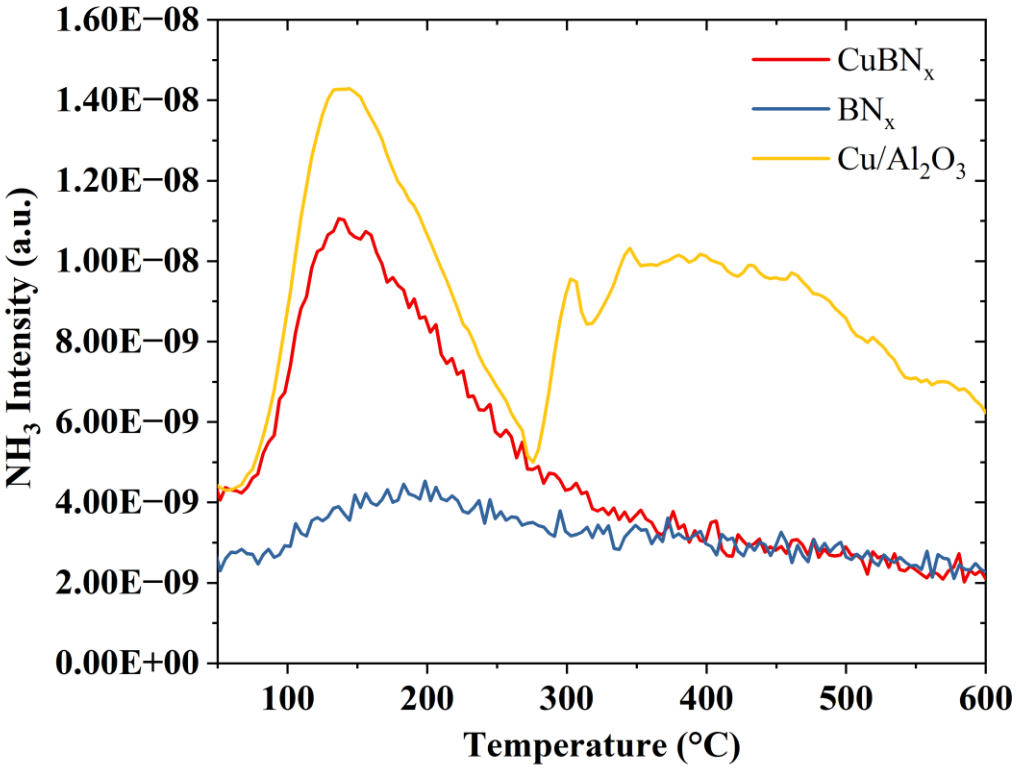

Figure 3.5 NH_3-TPD results of $CuBN_x$ and Cu/Al_2O_3.

Table 3.1 NH_3 Productivity of Al_2O_3 and Cu/Al_2O_3.

Catalysts	NH_3 productivity (μg/mg/h)
Al_2O_3	12.86
$CuAl_2O_3$	27.35

Besides, the SEM-EDS was used for the determination of elemental dispersion on the surface. The SEM-EDS results of $CuBN_x$ are shown in Figure 3.6 and the SEM-

EDS results of Cu/Al_2O_3 are shown in Figure 3.7. The EDS results confirmed the high content of O on the surface. However, the Cu-O bonding alone is not preferred in the reaction since the NH_3 productivity is limited. Thus, it is the interaction between Cu, BN_x and O that plays a critical role in the reaction.

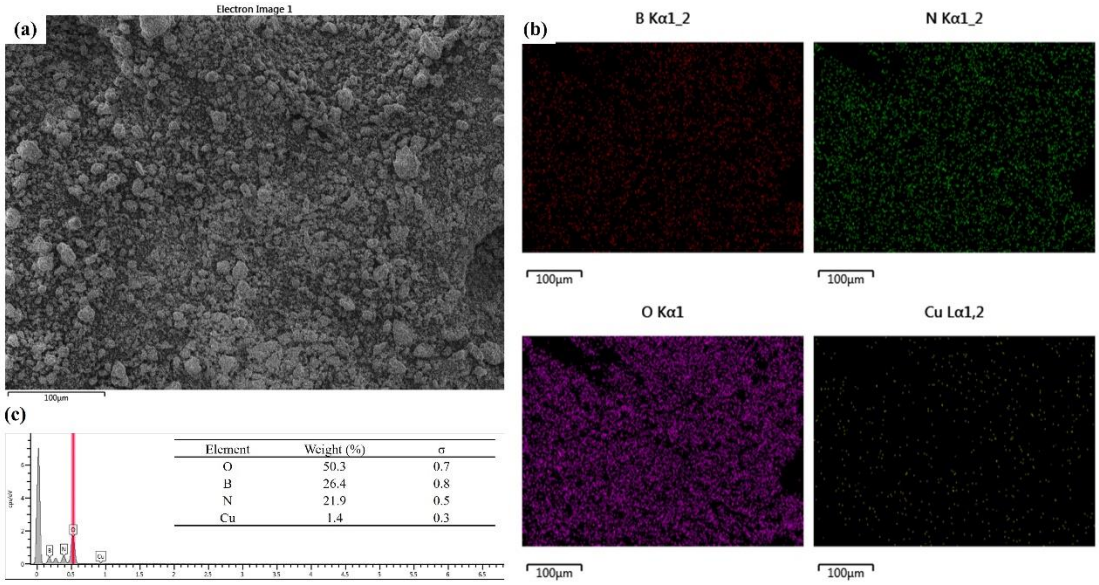

Figure 3.6 The SEM-EDS results of $CuBN_x$ (a) SEM image of $CuBN_x$; (b) elemental dispersion; (c) elemental dispersion.

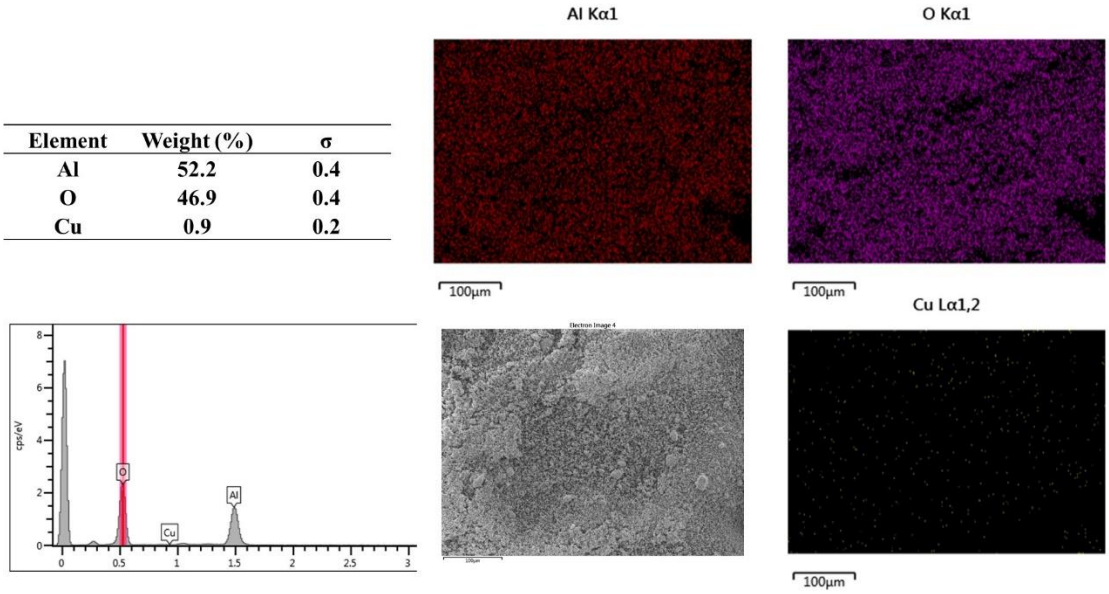

Figure 3.7 The SEM-EDS results of Cu/Al_2O_3.

The durability of $CuBN_x$-1wt-1:36 for NO_3RR was assessed by performing 150 minutes and five consecutive cycling tests as shown in Figure 3.8a, b. The NH_3 yield remains stable within 150 minutes test and five cycles without significant decreasing of the NH_3 productivity and the selectivity of NH_3 maintains over 95% after the cycling test.

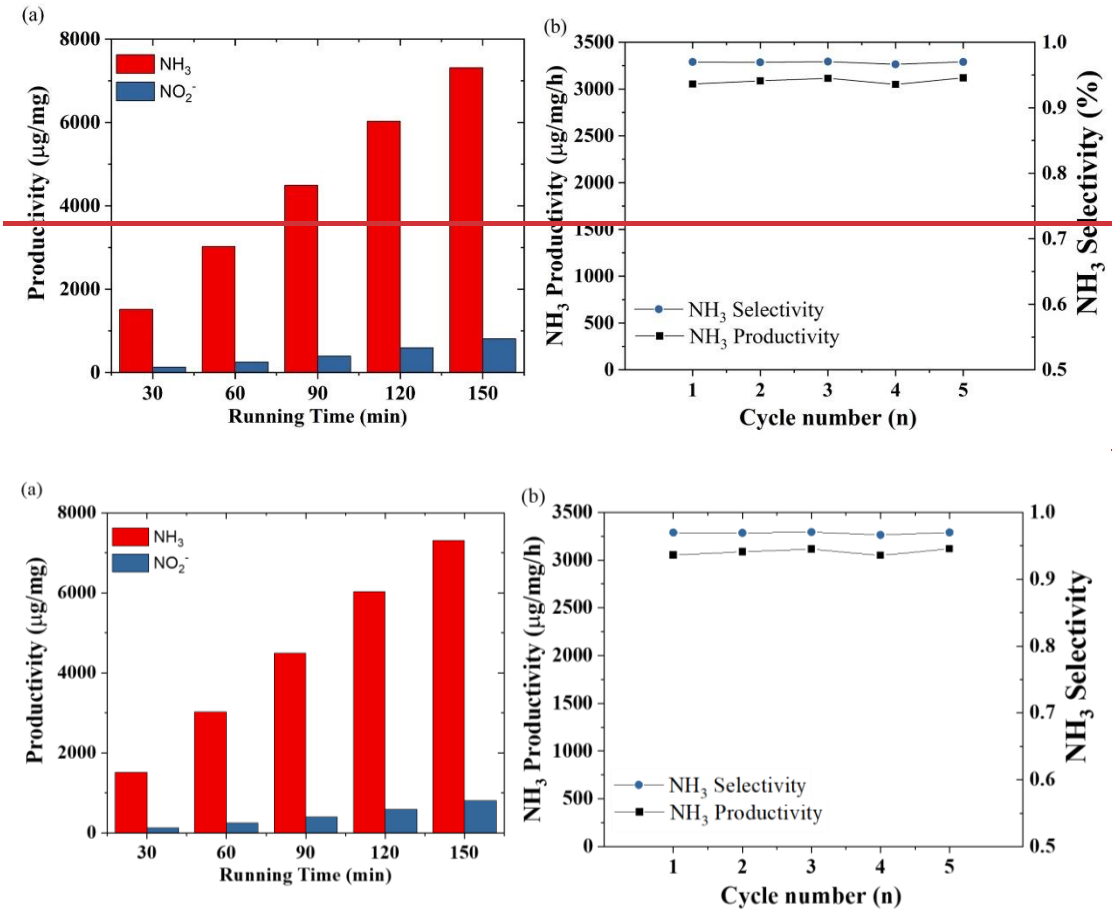

Figure 3.8 The stability test of $CuBN_x$-1wt-1:36 sample (a) 150minutes NO_3RR test with sampling every 30 minutes; (b) the repetitive tests of NO_3RR.

Table 3.2. BET surface area measurement and the NO_3RR activity.

Sample	BET area (m^2/g)	NH_3 Productivity (μg/mg/h)

BN_x	50.21	78.5
$CuBN_x$-0.5wt	44.67	1760.4
$CuBN_x$-0.75wt	43.69	2817.59
$CuBN_x$-1wt	43.66	3184.9
$CuBN_x$-2wt	15.29	2532.9
$CuBN_x$-3wt	12.58	1726.67

3.4 Summary

In conclusion, we have demonstrated that the $CuBN_x$ catalysts with single Cu atoms stabilized by porous boron nitride obtain promising activity in promoting NO_3RR at appreciably higher production rate of NH_3 under optimized Cu loading and B/N ratio. The formation of boron sites is the origin of the activity for porous BN. However, the performance of porous BN is not promising. After doping of Cu atoms, the Cu atoms were stabilized as the single atomic sites and promoted the NO_3RR performance with superior productivity and selectivity. XRD and XAS characterization further confirmed the isolation of Cu atoms. In addition, by comparing with the Cu/Al_2O_3 catalysts which even have a stronger Lewis's acidity and abundant Cu-O bonding, the $CuBN_x$ is still performing better. Thus, the interaction between BN, Cu and O is critical Besides, the XAS data also implies the preference of higher oxidation state of Cu in the reaction, in the following section, increasing oxidation state of Cu is considered a feasible strategy to further improve the reaction rate. In the next section, the surface elements distribution

will be investigated to reveal the role of different species and further improve the activity.

CHAPTER 4

OXYGEN ENHANCED $CuBN_x$ CATALYSTS FOR NO_3RR

4.1 Introduction

To date, researches have reported that palladium (Pd)[142, 143], platinum (Pt)[144, 145], copper (Cu)[146, 147], iron (Fe)[148], ruthenium (Ru)[149], nickel (Ni)[89], silver (Ag)[150], and cobalt (Co)[151], etc. are active as cathode materials for NO_3RR. It is noteworthy that the d-orbital energy levels of some metals (e.g., Cu, Ag, Pt) with highly occupied d-orbitals are similar to the lowest unoccupied molecular π* orbital (LUMO π*) of NO_3^-, and thus the electron transfer on these metals are promoted[152]. Compared with other metals, Cu shows the fastest rate determining steps of nitrate to nitrite and highest electrocatalytic reduction kinetics in NO_3RR[153]. Cu also offers higher exchange current densities and yield rate under strongly acidic conditions for NO_3RR[154]. With the advantages of low cost, weak hydrogen evolution ability, and strong electrical conductivity, Cu-based catalysts turn out to be outstanding in electrochemical NO_3RR[79, 155].

For transition metal electrocatalysts, while surface metal was traditionally considered to be the active site, anionic species such as anion doping, oxygen vacancy, hydroxyl group, proton on the surface were recently reported to actively participate in surface reactions. For instance, Wang et al. reported that oxygen vacancies on the surface of Co_3O_4 led to the formation of Co–OH* intermediate species, which were believed to play a critical role for oxygen evolution reaction (OER)[156]. Zhu et al. modulated the proton conductivity of double perovskite oxides thin film by crystal

orientation and observed strongly modified proton-coupled electron transfer process during OER[157]. Zheng et al. reported that oxygen vacancy-rich surface can regulate the binding affinities of CuOx to *CO, *COH and *CH2 intermediates, leading to enhanced CO_2 reduction reaction (CO_2RR) activity[158]. Roldan Cuenya et al. revealed that oxygen species in the surface and subsurface regions of Cu and Cu-derived oxides played a critical role in determining the hydrocarbon selectivity in CO_2RR, which were even more important than the presence of Cu low-index facets[159]. All research demonstrates that tuning surface oxygen species is a promising approach for improving the electrocatalytic activity of Cu catalysts towards NO_3RR.

Plasma treatment has been considered as an environmentally friendly and highly efficient technique for surface modification[160]. And this process can be carried out at room temperature without additional chemical reagents. In this work, we reported a one-step O_2 plasma treatment strategy to regulate the surface oxygen state of Cu electrocatalyst for strongly enhanced NO_3RR performance. The combination of XRD, FTIR, XAS and TPR results suggested that higher oxygen state of Cu after plasma treatment. As a consequence of such changes in surface Cu species, the $OCuBN_x$ exhibited a significant improvement in conversion rate for NO_3RR. The optimized NH_3 productivity increased from 3200 to 4029 $\mu g/h/g_{cat}$ with outstanding selectivity.

4.2 Experimental

In this section, porous BN_x supported copper single atom catalysts were prepared with different metal loading by pyrolysis method. Then, the as prepared samples were treated

in Oxygen-Plasma as $OCuBN_x$ samples. The properties of the catalysts were examined by using Brunauer-Emmett-Teller (BET), temperature-programmed reduction (TPR), Fourier-transform Infrared (FTIR) spectroscopy, XRD, scanning electron microscope (SEM), and X-ray absorption spectra (XAS). The catalytic of $OCuBN_x$ catalysts in NO_3RR was conducted in a self-designed H-Cell to investigate the effect of Cu loading and oxygen-plasma treatment on their catalytic performance.

4.2.1 $OCuBN_x$ synthesis

All the materials and chemicals were commercially available and were used without further purification. Preparation of BN_x: The intermediates consisted of a mixture of urea and boric acid that the boric acid was first dissolved in 80mL of DI water. Then a certain amount of urea was added to the solution. The mixer was further dried at 75 ℃ for 20 hours. The molecular ratios of urea and boric acid are equal to 1:36 based on our previous experimental results. These were selected as they enabled the production of porous BN_x while obtaining a good porosity and stability after high-temperature treatment. After drying the urea and boric acid, the mixture was heated at 600 ℃ for 4 hours with the protection of N_2 gas (30sccm).

Preparation of $CuBN_x$: The intermediates consisted of a mixture of urea and boric acid dissolved in DI water with the same procedure of the synthesis of BN. Then a certain amount of Cu precursor was added into the solution slowly with vigorous stirring. After drying, the mixture was heated at 600 ℃ for 4 hours with the protection of N_2 gas (30sccm). Then the sample was collected and grinded for the NO_3RR test and characterizations.

Plasma treatment: The fresh prepared sample was dispersed in the large alumina boat with very well dispersion. Then, the boat was placed in the plasma system (at the center of the plasma coil). Then the vacuum pump started to reach high level vacuum with flowing of necessary gas (15sccm). The power of RF-Plasma generator was pre-tuned to 125W. Then the sample was treated in plasma for a certain time.

4.2.2 $OCuBN_x$ characterization

BET surface area measurement: The specific surface areas were calculated by Brunauer-Emmett-Teller (BET) method on Micromeritics AutoChem 2920 automated characterization system (Micromeritics). Adsorption at liquid nitrogen temperature was performed using a 30% N_2/He stream, and the desorption area obtained after rapid heating was compared with the area of a calibrated volume. The amount of desorbed nitrogen molecules was used for the surface calculation.

TPR: TPR was used to reduce Cu species of catalyst. It was carried out in the AutoChem 2920 automated characterization system (Micrometrics) equipped with a thermal conductivity detector (TCD). The thermal conductivity detector was used to measure H_2 consumption during TPR experiment. An ice water trap was used to remove moisture from the TPReffluent stream before the TCD. 100 mg of sample was generally loaded in a quartz U-tube. The TPR was performed using 30mL/min of 10 vol.%H_2/Ar from room temperature to 600 ℃ at a heating rate of 10 ℃/min and TCD signal was recorded by an online computer.

FTIR: FTIR was carried out using a Nicolet ThermoElectron FTIR 560 spectrometer together with a MIRacle attenuated total reflectance (ATR) platform

assembly and a Ge Plate. The scanning range was between 700 and 4000 cm^{-1}, and the scanning time was 32 s. Spectra were acquired at 2 cm^{-1} resolution.

XRD: In order to get the crystal information, powder XRD patterns were recorded monochromatic Cu Kα radiation (λ = 1.5406 Å). XPS data was obtained from a Thermo Scientific ESCALAB 250Xi with a monochromic Al Kαradiation.

SEM: The scanning electron microscopy images were obtained using a field emission environmental scanning electron microscope (SEM, JEOL, JSM-7900F).

XAS: XAS data were processed with Demeter (v.0.9.26). Using Athena software in Demeter, XAS spectral was performed with normalization using a cubic spline function that was used to fit the background above the absorption edge. 2 Then, the data was transformed to the normalized EXAFS function, χ(E), in energy space to χ(k), where k is the photoelectron wave vector. χ(k) was multiplied by k2 to amplify the EXAFS oscillations in the mid-k region for assessing the interatomic interaction of Cu atoms. To differentiate the EXAFS oscillation from different coordination shells, Fourier transformation (from k space to R space) of the k2 −weighted χ(k) with a k range of 3 − 11.5 Å−1 for the Cu K−edge was conducted. Subsequently, EXAFS data recorded in R space was fitted using Artemis software in Demeter with the FEFF6 program. The Cu first shell was fitted at an R range of 1.6 − 3.2 Å. The phase and amplitude functions of Cu−O and Cu−Cu were calculated with FEFF. A S0 value of 0.80 for Cu was determined from Cu foil, which was then applied to the Cu K−edge EXAFS fittings of the samples. From these standard EXAFS fitting practices, structural parameters of Cu samples were calculated, including coordination number (CN), bond

distance (R), inner potential shift (ΔE), and Debye-Waller factor (σ2).

4.2.3 Catalyst test and products analysis

Electrocatalytic reduction of nitrate: A three-electrode sealed H-type cell was used in all electrochemical tests. Catalysts (50 mg) were dispersed in a solution of ethanol (0.3 mL), and 5 wt.% Nafion solution (0.011 mL). After sonication for 4 min, a uniform ink-like dispersion was obtained. Next, 11 μL of the dispersion was dropped onto a polished glassy carbon electrode (GCE), and the resulting electrode was allowed to dry in air for half an hour. This catalyst/GCE served as the working electrode in subsequent electrochemical tests. An Ag/AgCl electrode and a Pt wire were used as the reference electrode and the counter electrode, respectively. The electrochemical nitrate reduction was performed by chronoamperometry with the potential ranging between 0V and -1.3V to obtain the reduction efficiency and the distribution of products under various conditions.

Determination of nitrite: Nitrite-N was determined using Griess reagent as the color reagent. First, mix equal volumes of N-(1-naphthyl) ethylenediamine (Component A) and sulfamic acid (Component B) to form the Griess Reagent. Prepare sufficient reagent for immediate experiments only (100 μL per spectrophotometer cuvette). Next, 0.3mL was taken out from the electrolytic cell and diluted to 2.9mL in the cuvette followed by mixing 0.1 mL of prepared Gress's Reagent. Then, incubate the mixture for 30 minutes at room temperature. The absorption intensity at a wavelength of 548 nm was recorded for further determination. The concentration-absorbance curve was calibrated using the standard nitrite-containing solution provided by the

manufacturer.

Determination of ammonia: Ammonia-N was determined using Nessler's reagent as the color reagent. First, 0.3 mL of electrolyte was taken out from the electrolytic cell and diluted to 2.7 mL in the cuvette. Next, 0.2 mL potassium sodium tartrate solution (ρ=500 g/L) was added and mixed thoroughly, then 0.1 mL Nessler's reagent was added into the solution. The absorption intensity at a wavelength of 420 nm was recorded after sitting for 30 min. The concentration-absorbance curve was calibrated using a series of standard ammonium chloride solutions and the ammonium chloride crystal was dried at 75℃ overnight in advance.

Determination of nitrate: Nitrate-N was determined using the Nitrate kit from HACH company without any further treatment. First, a certain amount of electrolyte was taken out from the electrolytic cell and diluted 40 times. Then, 0.2mL of the diluted electrolyte solution was added to the sample container provided with the nitrate kits. Next, 1mL of solution A was added to the sample container and shaken for 2 seconds. After waiting for 15 minutes, the absorbance was detected at 345 nm. The concentration-absorbance curves were calibrated using a series of standard sodium nitrate solutions. The sodium nitrate was dried at 75℃ overnight in advance.

Calculation of related indicator:

The NO_3^-conversion can be calculated by the equation as follows:

$$NO_3^-\text{conversion} = \frac{\Delta c_{NO_3^-}}{c_0} \times 100\% \qquad (4.1)$$

The initial concentration of NO_3^- is marked as c_0 (μg/mL), and the concentration of NO_3^- after the reaction is marked as $c_{NO_3^-}$ (μg/mL).

The concentration of NH_3-N and NO_2^- after the reaction is marked as c_{NH_3} and $c_{NO_2^-}$, respectively (μg/mL). The selectivity of NH_3 can be calculated by the equation as follows:

$$\mathrm{NH_3\ selectivity} = \frac{\mathrm{c_{NH_3}}}{c_{NH_3} + c_{NO_2^-}} \times 100\% \tag{4.2}$$

The Faradaic efficiency of NH_3 can be calculated by the equation as follows:

$$\mathrm{FE_{NH_3}} = \frac{\mathrm{n \cdot F \cdot c_{NH_3} \cdot V}}{\mathrm{M_{NH_3} \cdot Q}} \times 100\% \tag{4.3}$$

n represents the number of electrons transferred from nitrate to ammonia, here it is 8. V represents the volume of electrolyte (mL). In our electrochemical test, the left cell contains 50mL electrolyte, so V here is 50mL. $\mathrm{M_{NH_3}}$ represents the relative molecular mass of NH_3. Q represents the total charge transferred in the entire reaction. F is the Faradaic constant, which is 96485 C/mol. Therefore, the Faradaic efficiency of NH_3 can be calculated by the equation as follows.

4.3 Results and Discussion

4.3.1 Structural characterization

The $CuBN_x$ catalysts were synthesized via pyrolysis method in an inert environment. The crystalline structure and chemical state of $CuBN_x$ and oxygen plasma treated $CuBN_x$ ($OCuBN_x$) samples were identified by XRD. Figure 4.1a shows that the $CuBN_x$-1wt sample and BN_x exhibited only a broad peak at 26° and 42° assigned to the formation of porous BN_x. No characteristic peaks were detected for metallic Cu. Conversely, for the $CuBN_x$-2wt sample, there are two characteristic peaks at 43° and 50°, assigned to the (111) and (200) planes of the cubic phase of Cu, respectively. This

indicates the presence of Cu particles. Furthermore, the effect of oxygen plasma on $CuBN_x$ sample was also characterized by XRD. As shown in Figure 4.1a, the formation of B_2O_3 was confirmed that the peaks at 15° and 29° are the two characteristic peaks for B_2O_3[161]. The FTIR results also implied the formation of B-O bonding on the surface[162]. As shown in Figure 4.1b, the peaks at 1185 cm^{-1}, 1389 cm^{-1} and 3177 cm^{-1} correspond to boric anhydride B_2O_3[163]. However, the formation of metallic Cu was undetectable in XRD.

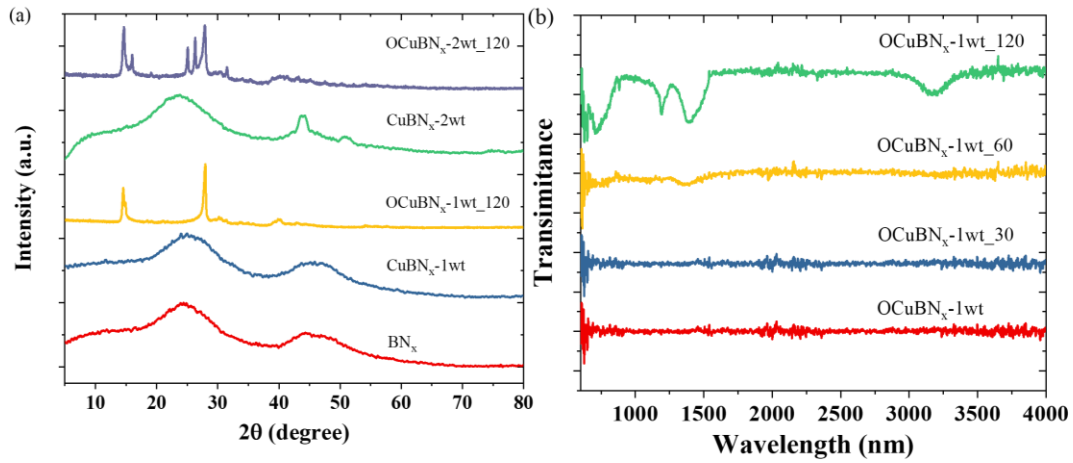

Figure 4.1 XRD and FTIR characterizations (a) XRD; (b) FTIR results of $OCuBN_x$ samples.

To further investigate the chemical environment of $OCuBN_x$-1wt sample, X-ray absorption near edge structure (XANES) and extended X-ray absorption fine structure (EXAFS) were performed. The chemical environment of Cu atoms has been determined by X-ray absorption spectra (XAS) at the Cu K-edge as shown in Figure 4.2a. The near-edge spectra show features at 8981 (A), 8986 (B), 8993 (C), and 9002 eV (D), where the weak pre-edge peak A arising from the dipole-forbidden 1s → 3d transition can be employed to fingerprint the presence of Cu^{2+} with a d9 electronic configuration[133], and

the peak C is attributed to the 1s → 4p (continuum) electron transition of Cu^{2+} with the ligand effect on the transition rising as peak B[134], while peak D refers to the multiple scattering[135]. Furthermore, by comparing $CuBN_x$-1wt sample with $OCuBN_x$-1wt sample, $CuBN_x$-1wt_TPR and the Cu foil, the oxidation state of Cu was determined as the order: $OCuBN_x > CuBN_x > CuBN_x$_TPR. The preference of high Cu oxidation state in the NO_3RR was also reported by other groups[136].

The local coordination structure of $CuBN_x$, X-ray absorption fine structure (XAFS) was further investigated with Cu foil as references, as shown in Figure4.2b. The Fourier-transformed extended X-ray absorption fine structure (FT-EXAFS) spectrum of $CuBN_x$-1wt samples shows a peak at 1.41 Å, which can be assigned to Cu−BN interaction[137-139]. Such results imply that the isolated Cu atoms are well-dispersed on the porous support. As for $CuBN_x$-1wt_TPR, a main Cu−Cu characteristic peak can be detected at 2.20 Å, confirming the expected Cu clustering in the sample [133, 134]. On the contrary, there is no Cu-Cu bonding detected from $OCuBN_x$-1wt, which implies the isolation of Cu atoms after long time oxygen plasma treatment.

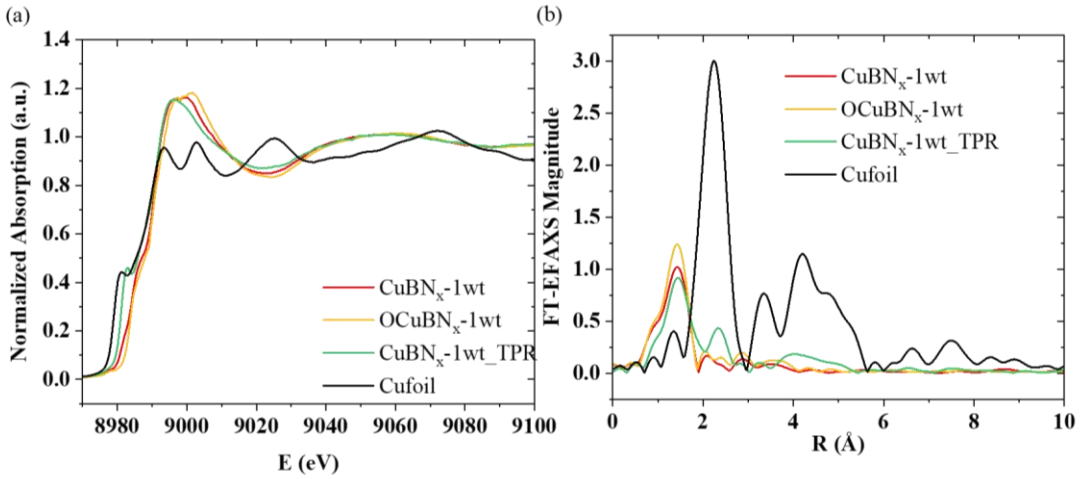

Figure 4.2 X-ray absorption results (a) Cu K-edge XANES spectra; (b) FT-EXAFS spectra.

The TPR experiments were further conducted to confirm the effect of oxygen plasma treatment. As shown in Figure 4.3, the Cu species were reduced at 366 °C, such a high reduction temperature was due to the strong interaction between Cu atoms and substrates which is also proved by XAS results. Compared with oxygen plasma treated sample, the reduction temperature increased about 26 (from 366 °C to 392°C), which is due to the higher oxidation state of Cu and maybe stronger metal-support interaction. Besides, there is another reduction peak of $OCuBN_x$ sample at 497 °C which can be assigned to the reduction of B_2O_3 species[164].

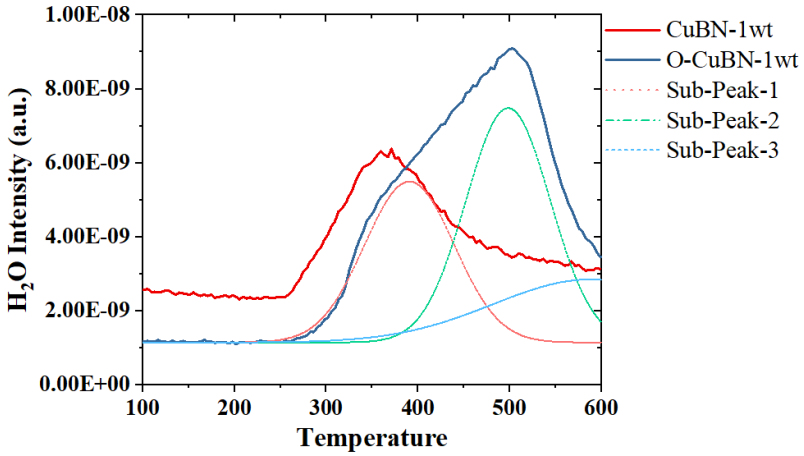

Figure 4.3 Temperature programmed reduction of $CuBN_x$ and $OCuBN_x$ samples.

The SEM-EDS was also used to identify the species on the samples. The results of $CuBN_x$ are shown in Figure 4.4, the results of $OCuBN_x$ are shown in Figure 4.5 and the results of $CuBN_x$-N_2 plasma are shown in Figure 4.6. By comparing with the content of O species (Figure 4.4c, Figure 4.5c and 4.6c), it is clear that the higher content of O element was detected for $OCuBN_x$ samples after oxygen plasma

treatment and lower content of O after N_2 plasma treatment. Besides, the content of Cu increased as well after the oxygen plasma treatment.

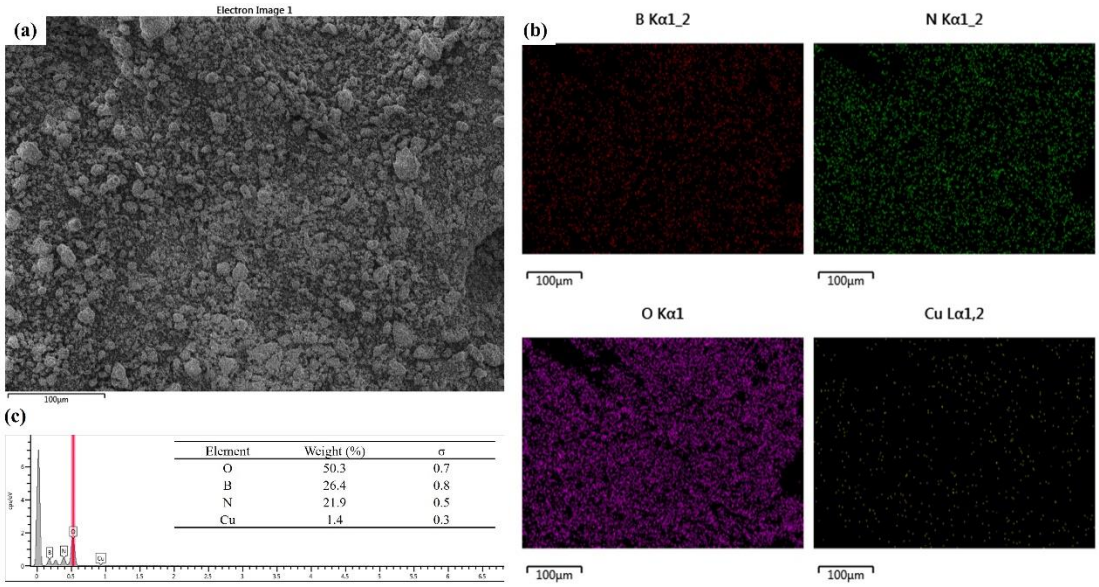

Figure 4.4 The SEM-EDS results of $CuBN_x$ (a) SEM image of $CuBN_x$; (b) elemental dispersion; (c) elemental dispersion.

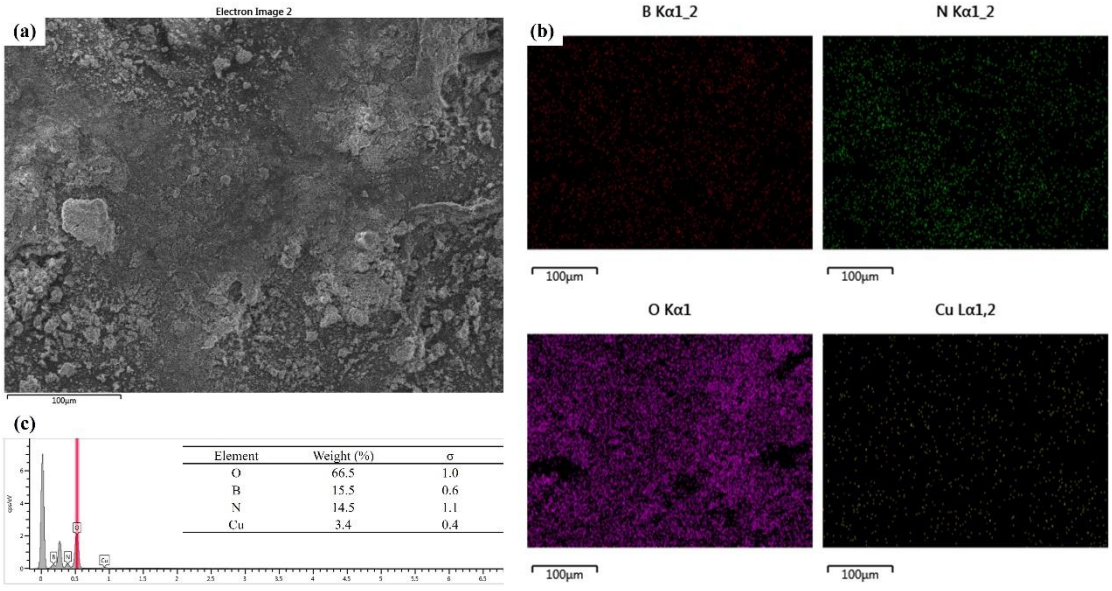

Figure 4.5 The SEM-EDS results of $OCuBN_x$ (a) SEM image of $CuBN_x$; (b) elemental dispersion; (c) elemental dispersion.

4.3.2 Catalytic performance.

The NO_3RR activity of the catalysts was tested in a two-compartment H-cell system. The concentration of NO_3^-, NH_3 and NO_2^- were determined via the UV-vis spectrophotometry. The calibration curves are shown in Figure 4.6. To evaluate the catalytic performance of $CuBN_x$ samples and the effect of oxygen plasma, the electrochemical performance of $CuBN_x$ and $OCuBN_x$ samples were examined and compared. The current due to the transportation of electrons resulting in higher current with lower potentials applied as shown in Figure 4.7a. As shown in Figure 4.7b, the NH_3 productivity increased while the $CuBN_x$ was treated in oxygen plasma for longer time (from 3189 to 4029 $\mu g/h/mg_{cat}$ after 120 minutes treatment).

However, the NH_3 productivity decreased dramatically when the $CuBN_x$ was treated for 150 mins in oxygen plasma. The BET measurement indicates a significant decreasing of surface area for the $OCuBN_x$ sample treated for 150 minutes, which is resulted from agglomeration of porous BN structure caused by the heat radiation from plasma as shown in Table 4.1. Even though the surface area decreased slightly, the catalysts still provide enough surface-active sites to maintain a high reaction rate.

Besides, the productivity of NO_2^- was exhibiting a similar pattern with NH_3, which implies the NO_3RR passes through a $2e^-$ pathway and the NO_2^- is the intermediate. The $CuBN_x$ and $OCuBN_x$ samples were also compared with different metal loading to obtain deeper understanding of the reaction (NO_3RR tested at -0.7 Vs. SCE). As shown in Figure 4.7c, the $CuBN_x$ and $OCuBN_x$ exhibited a volcano shape of NH_3 productivity with higher Cu loading (from 0.5wt% to 3.0 wt.%). The 1wt.% loading of Cu is considered the optimized Cu loading that can maintain the atomic dispersion of Cu on

the surface and serve as the active sites. The higher NH_3 productivity originated from a higher oxidation state of Cu.

On the other hand, the productivity of NO_2^- on $CuBN_x$ samples increased with higher Cu loading which is contrary with the $OCuBN_x$. The increased NO_2^- productivity for $CuBN_x$ sample and decreased NH_3 productivity may have resulted from the formation of metallic Cu which is easier for NO_2^- species to desorbed from the surface and preventing the further reduction steps to NH_3. The decrease of the overall activity, NH_3 productivity and NO_2^- productivity, is due to the agglomeration of porous BN_x.

By comparing $CuBN_x$ and $OCuBN_x$ samples, it is concluded that the higher oxidation state of Cu is preferred for the formation of NH_3 by providing a stronger absorption of NO_2^- for following reduction pathways. The comparison of $CuBN_x$ and $OCuBN_x$ with Cu loading of 1wt% is shown in Figure 4.7d. The decreasing of NH_3 productivity at high potential range is due to the dominance of competing reaction of HER[132]. However, the OCuBN samples still maintained higher NH_3 selectivity than $CuBN_x$ sample at high potential range, which is also due to a stronger absorption of NO_2^- intermediates on Cu species with higher oxidation state.

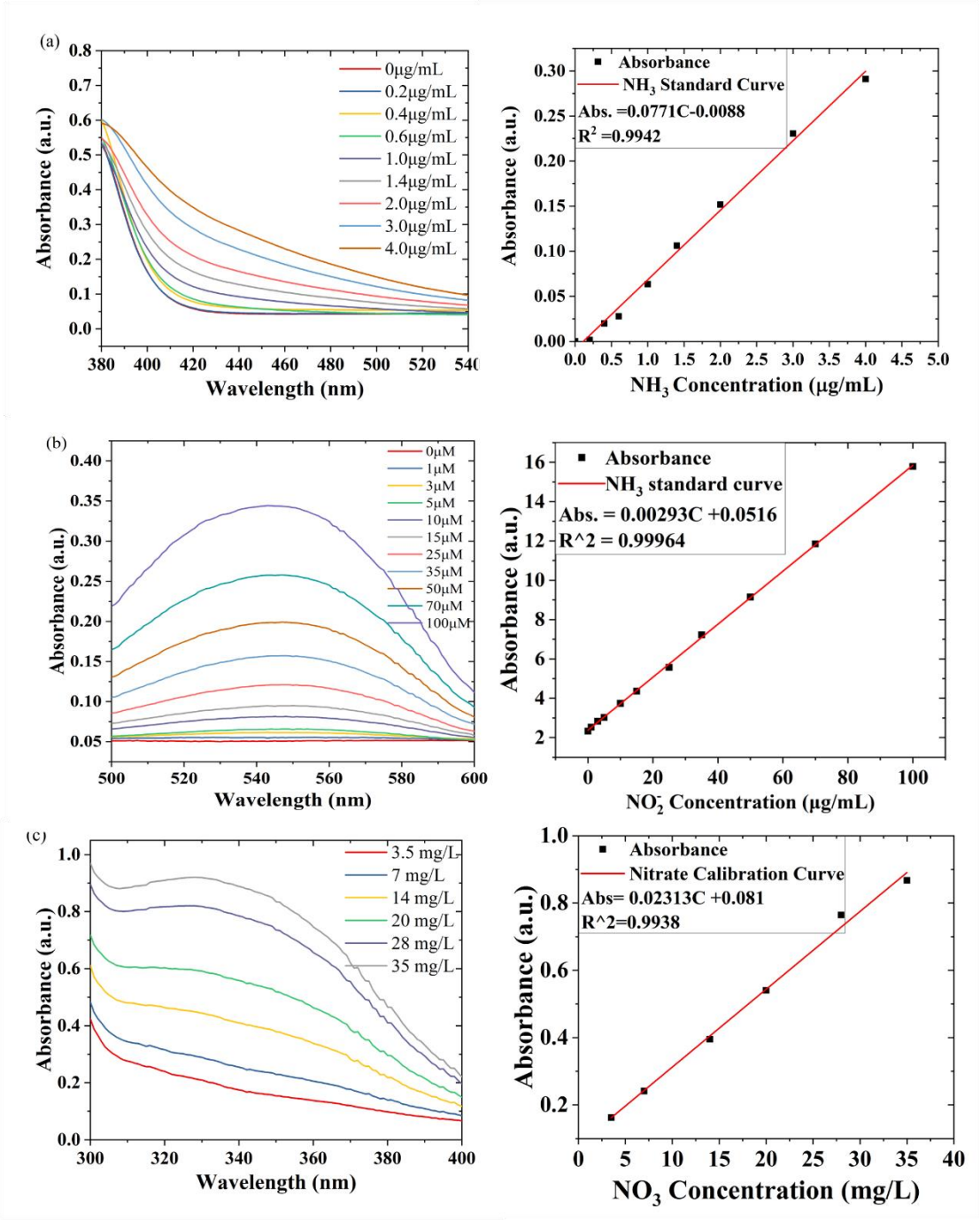

Figure 4.6 Calibration curve for determination of products (a) NH_3; (b) NO_2^-; (c) NO_3^-.

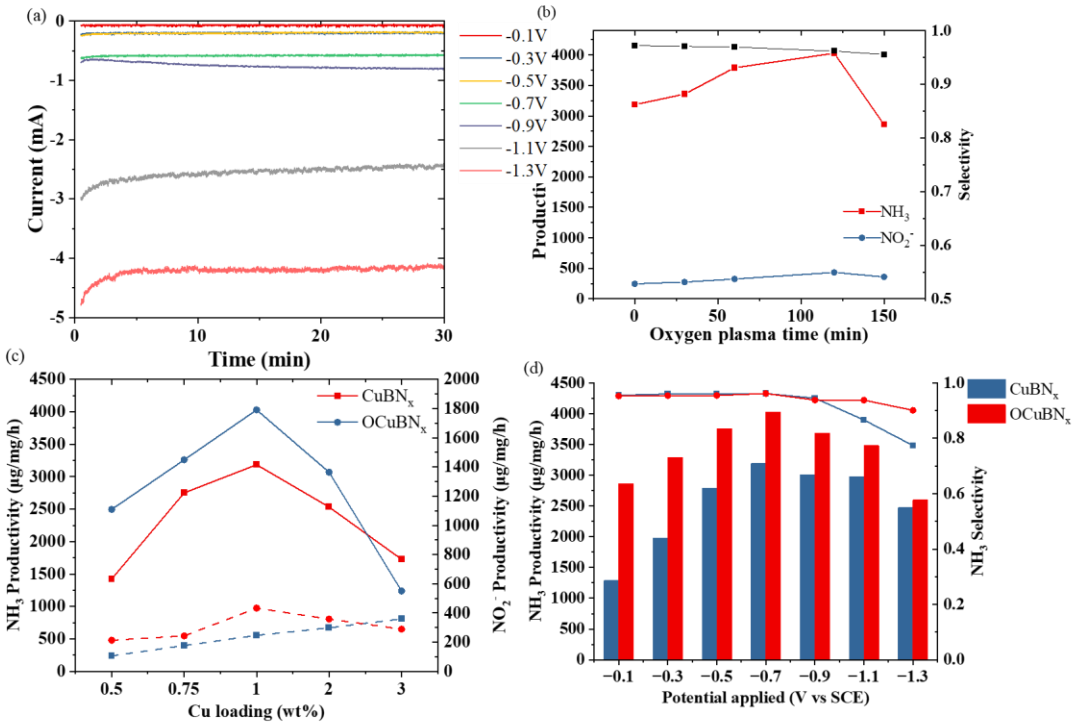

Figure 4.7 The catalytic performance of $CuBN_x$ and $OCuBN_x$ samples (a) current collected at different potentials for $OCuBN_x$ sample; (b) the effect of plasma treatment on catalytic performance; (c) the comparison of $CuBN_x$ sample and $OCuBN_x$ sample with different Cu loading; (d) the comparison of $CuBN_x$ sample and $OCuBN_x$ (1 wt.% Cu loading) sample at different potentials.

Table 4.1 BET Area of $OCuBN_x$ Samples and NO_3RR Activity

Sample	BET area (m^2/g)	NO_3RR activity ($\mu g/h/mg_{cat}$)
BN_x	50.21	78.5
$OcuBN_x$-0.5wt	35.76	2495.4
$OcuBN_x$-0.75wt	27.58	3259.4
$OcuBN_x$-1wt	24.34	4029.5
$OcuBN_x$-2wt	17.57	3068.5
$OcuBN_x$-3wt	10.35	1239.6

However, it is too early to conclude that higher content of oxygen species on the surface is the only origin of the improved activity since the Cu content also increased after the oxygen plasma treatment. Thus, the N_2 and Ar plasma were used to tune the element distribution on the surface and the O_2-TPO treated sample was also prepared as comparison. The ammonia productivity was tested at -0.7V vs SCE. The NH_3 productivity and the selectivity are shown in Table 4.2. By comparing the $CuBN_x$, $OCuBN_x$ and $CuBN_x$-O_2TPO samples, it is clear that even though the oxygen plasma improved the oxygen concentration on the surface. The oxygen is not the origin of the activity, since the Cu concentration is much higher after oxygen plasma treatment. Then, by comparing the O_2 plasma, N_2 plasma and Ar plasma treated sample, it is clear that the Cu concentration are similar, but only O_2 plasma treated sample obtained higher performance. This comparison proved the critical role of oxygen again. Thus, it is reasonable to conclude that the complex interaction of Cu, BN and O is critical to the reaction. The SEM results of N_2 and Ar plasma treated sample are shown in Figure 4.8 and Figure 4.9 and the SEM results of $CuBN_x$-TPO are shown in Figure 4.10.

Table 4.2 Plasma Effect on $CuBN_x$ Catalysts

Treatment	NH_3 yield (μg/h/mg_{cat})	NH_3 selectivity	BET area (m^2/g)
No plasma	3190	0.961	43.66
O_2 plasma	4029.5	0.962	24.34
N_2 plasma	2989.7	0.947	25.67
Ar Plasma	2993.1	0.950	24.82
O_2-TPO	2058.4	0.941	17.38

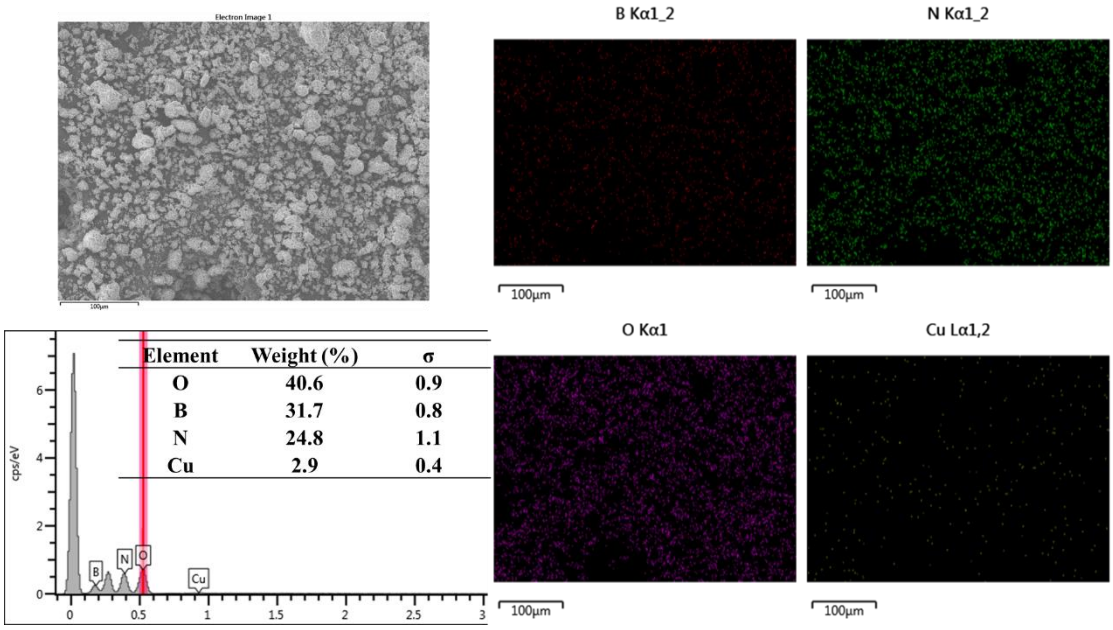

Figure 4.8 The SEM-EDS results of N_2-plasma treated $CuBN_x$.

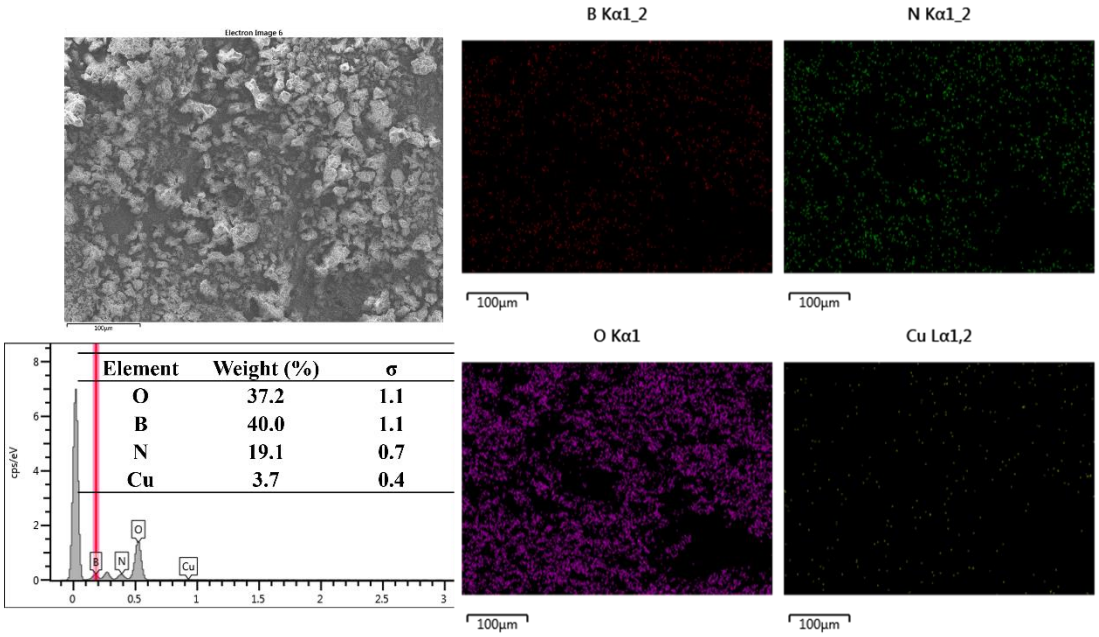

Figure 4.9 The SEM-EDS results of Ar-plasma treated $CuBN_x$.

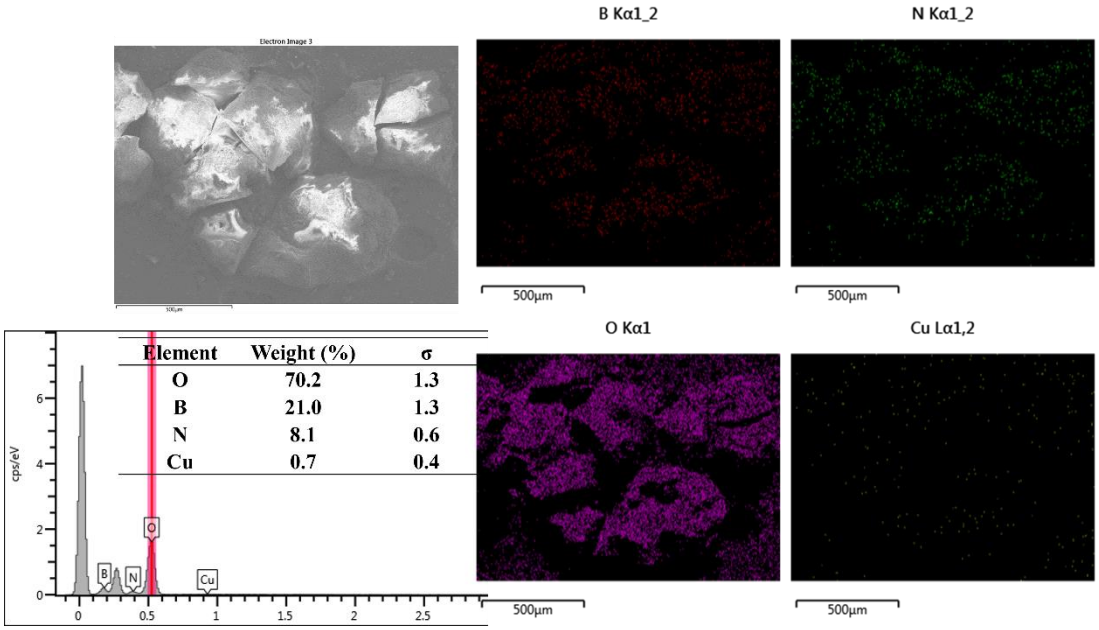

Figure 4.10 The SEM-EDS results of $CuBN_x$-TPO.

4.4 Summary

In this section, we have successfully improved the catalytic performance of $OCuBN_x$ sample by using O_2 plasma treatment. The $CuBN_x$ catalysts were treated in O_2 plasma,

N_2 plasma and Ar plasma to investigate the effect of plasma and optimize the performance. The results imply that only O_2 plasma has a positive effect on the reaction rate and the NH_3 productivity increased to 4029.5 μg/h/mg_{cat} with outstanding selectivity. The improved activity is due to the complex interaction between Cu, BN_x and O species on the surface. On the contrary, there is a slight decrease of the performance for the $CuBN_x$ after N_2 and Ar plasma treatment, which is due to the losing of oxygen species on the surface and compromised the interaction between Cu, BN_x and O. This section successfully proved the synergic effect of Cu, BN_x and O. The optimized ratio of these three elements may further improve the performance.

CHAPTER 5

CONCLUSION AND PERSPECTIVES

In this work, we have developed a pyrolysis method for the synthesis of $CuBN_x$ with abundant Cu-BN_x sites on the surface and tunable oxidation state of Cu for electrochemical ammonia synthesis. The optimized NH_3 productivity obtained 118.3 and 4029.5 $\mu g/h/mg_{cat}$ in NRR and NO_3RR, respectively. The XRD and XAS results proved the formation of isolated Cu atomic sites on the surface and serving as the active sites. Besides, the oxidation state of Cu plays an important role in the reaction. By using O_2 plasma treatment, the oxidation state of Cu was tuned to further improve the activity.

Major conclusions and achievements from the result of this work are:

1. The pyrolysis method was used to synthesis porous BN_x supported transition metal-based catalysts. The effect of metal loading, B/N ratios were investigated and the optimized synthesis procedure were developed with highest content of Cu single atomic sites on the surface.

2. The catalytic performance was tested for NRR and NO_3RR with outstanding activity and stability. The product analysis results showed that the HER is the competing reaction in both reactions. Besides, for the NO_3RR, the NO_2^- is a key intermediate in the reduction pathway, and the reduction of NO_2^- is the rate limiting step at high potential range.

3. The chemical environment of Cu atoms was investigated by XRD, XAS, TPD and H_2-TPR. The XRD and XAS results indicated the formation of isolated Cu atoms, and XANES results showed the preference of higher oxidation state of Cu in NO_3RR.

4. O_2 plasma was used to tune the oxidation state of Cu after the synthesis of $CuBN_x$ samples without destroying the porous structure of BN. A higher NH_3 productivity in NO_3RR was obtained $OCuBN_x$ samples, which further proved our assumption mentioned above.

5. The synergic effect of Cu, BN_x and O is critical for the NRR and NO_3RR reactions, the complex electron hybridization between the Cu, BN_x and O species may tune the adsorption energy for reactants and intermediates.

Although there is a significant improvement of NH_3 productivity in this work. The activity is still undesirable for a real application. In the future there are more efforts that should be made to improve the yield. The nitrogen cycle is shown in Figure 5.1 to guide the future study in this area and several tasks for the future work are summarized below.

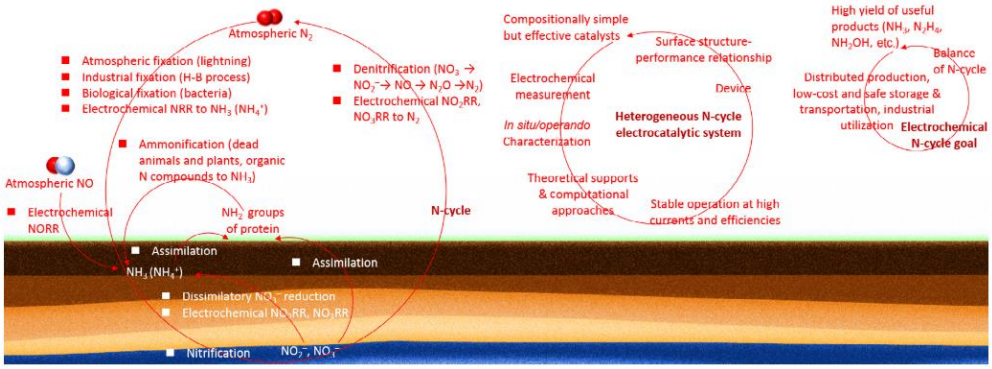

Figure 5.1 Challenges and goals in N-cycle electrocatalysis. From left to right: (a) key transformation steps within N-cycle, (b) challenges and goals in current electrocatalytic conversion of nitrogen species, (c) higher goals.

1. Despite widespread interest in SACs for N-cycle electrocatalysis, their true structures for catalytic conversions are difficult to identify. Meanwhile, it is encouraged to investigate catalysts with hetero-diatomic M1–M2 sites or even hetero-triatomic M1-M2-M3 sites. However, for N-cycle electrocatalysis, the investigated diatomic catalysts are limited to Zn/Fe–N–C for NRR and PdCu/NC for NRR[165, 166]. In-depth investigation of some less studied materials in N-cycle electrocatalysis is expected to shed light on the design of new electrocatalytic systems.

2. Furthermore, the ocean is an incredibly nitrogen-rich reservoir, and using electrochemistry to electrify the N-cycle within the ocean would be an interesting research topic. Furthermore, it is possible to imagine the construction of coastal facilities (e.g., electrolyzer) for distribution NH_3 with more advanced technological tools to assist us.

3. Besides, the design of N-cycle reaction-based electrochemical reactors with new functions, including solar-powered NH_3-producting electrolyzer, metal-N_2 battery and metal-NO_3^- battery, is interesting and meaningful.

REFERENCES

1. Liang, S.; Hao, C.; Shi, Y., The Power of Single-Atom Catalysis. *ChemCatChem* **2015,** *7* (17), 2559-2567.

2. Zhu, C.; Fu, S.; Shi, Q.; Du, D.; Lin, Y., Single-atom electrocatalysts. *Angewandte Chemie International Edition* **2017,** *56* (45), 13944-13960.

3. Qiao, B.; Wang, A.; Yang, X.; Allard, L. F.; Jiang, Z.; Cui, Y.; Liu, J.; Li, J.; Zhang, T., Single-atom catalysis of CO oxidation using Pt 1/FeO x. *Nature Chemistry* **2011,** *3* (8), 634.

4. Tang, Y.; Wang, Y.-G.; Li, J., Theoretical investigations of Pt1@ CeO2 single-atom catalyst for CO oxidation. *The Journal of Physical Chemistry C* **2017,** *121* (21), 11281-11289.

5. Ma, S.; Kenis, P. J., Electrochemical conversion of CO2 to useful chemicals: current status, remaining challenges, and future opportunities. *Current Opinion in Chemical Engineering* **2013,** *2* (2), 191-199.

6. Back, S.; Lim, J.; Kim, N.-Y.; Kim, Y.-H.; Jung, Y., Single-atom catalysts for CO 2 electroreduction with significant activity and selectivity improvements. *Chemical Science* **2017,** *8* (2), 1090-1096.

7. Li, F.; Han, G.-F.; Noh, H.-J.; Kim, S.-J.; Lu, Y.; Jeong, H. Y.; Fu, Z.; Baek, J.-B., Boosting oxygen reduction catalysis with abundant copper single atom active sites. *Energy and Environmental Science* **2018,** *11* (8), 2263-2269.

8. Trofimovaite, R.; Parlett, C. M.; Kumar, S.; Frattini, L.; Isaacs, M. A.; Wilson, K.; Olivi, L.; Coulson, B.; Debgupta, J.; Douthwaite, R. E., Single atom Cu (I) promoted mesoporous titanias for photocatalytic Methyl Orange depollution and H2 production. *Applied Catalysis B: Environmental* **2018,** *232*, 501-511.

9. Song, P.; Luo, M.; Liu, X.; Xing, W.; Xu, W.; Jiang, Z.; Gu, L., Zn single atom catalyst for highly efficient oxygen reduction reaction. *Advanced Functional Materials* **2017,** *27* (28), 1700802.

10. Li, J.; Chen, S.; Yang, N.; Deng, M.; Ibraheem, S.; Deng, J. Li, J.; Li, L.; Wei, Z., Ultrahigh-Loading Zinc Single-Atom Catalyst for Highly Efficient Oxygen Reduction in Both Acidic and Alkaline Media. *Angewandte Chemie International Edition* **2019,** *58* (21), 7035-7039.

11. Hou, P.; Huang, Y.; Ma, F.; Zhu, G.; Du, R.; Wei, X.; Zhang, J.; Wang, M., Screening of single-atom catalysts of transition metal supported on MoSe2 for high-efficiency nitrogen reduction reaction. *Molecular Catalysis* **2023,** *537*, 112967.

12. Wang, S.; Gao, H.; Li, L.; San Hui, K.; Dinh, D. A.; Wu, S.; Kumar, S.; Chen, F.; Shao, Z.; Hui, K. N., High-throughput identification of highly active and selective single-atom catalysts for electrochemical ammonia synthesis through nitrate reduction. *Nano Energy* **2022,** *100*, 107517.

13. Aiken III, J. D.; Lin, Y.; Finke, R. G., A perspective on nanocluster catalysis: polyoxoanion and (n-C4H9) 4N+ stabilized Ir (0)∼ 300 nanocluster 'soluble heterogeneous catalysts'. *Journal of Molecular Catalysis A: Chemical* **1996,** *114* (1-3), 29-51.

14. Thielbeer, F.; Donaldson, K.; Bradley, M., Zeta potential mediated reaction monitoring on nano and microparticles. *Bioconjugate Chemistry* **2011,** *22* (2), 144-150.

15. Antonels, N. C., *The evaluation of dendrimer encapsulated ruthenium nanoparticles, immobilised on silica, as catalysts in various catalytic reactions and the effect of ionic liquids on the catalytic activity*. University of Johannesburg (South Africa): 2015.

16. Kidwai, M., Nanoparticles in green catalysis. *Handbook of Green Chemistry:***2010**, 81-92.

17. Lokteva, E. S.; Golubina, E. V., Metal-support interactions in the design of heterogeneous catalysts for redox processes. *Pure and Applied Chemistry* **2019,** *91* (4), 609-631.

18. Rozita, Y.; Brydson, R.; Scott, A. In *An investigation of commercial gamma-Al2O3 nanoparticles*, Journal of Physics: Conference Series, IOP Publishing: 2010; p 012096.

19. Lippits, M.; Iwema, R. B.; Nieuwenhuys, B., A comparative study of oxidation of methanol on γ-Al2O3 supported group IB metal catalysts. *Catalysis Today* **2009,** *145* (1-2), 27-33.

20. Pacchioni, G.; Freund, H.-J., Controlling the charge state of supported nanoparticles in catalysis: lessons from model systems. *Chemical Society Reviews* **2018,** *47* (22), 8474-8502.

21. Liu, G.; Tran-Phu, T.; Chen, H.; Tricoli, A., A review of metal-and metal-oxide-based heterogeneous catalysts for electroreduction of carbon dioxide. *Advanced Sustainable Systems* **2018,** *2* (8-9), 1800028.

22. Ahmad, T.; Liu, S.; Sajid, M.; Li, K.; Ali, M.; Liu, L.; Chen, W., Electrochemical CO 2 reduction to C 2+ products using Cu-based electrocatalysts: A review. *Nano Research Energy* **2022,** *1* (2), e9120021.

23. Thorseth, M. A.; Tornow, C. E.; Edmund, C.; Gewirth, A. A., Cu complexes that catalyze the oxygen reduction reaction. *Coordination Chemistry Reviews* **2013,** *257* (1), 130-139.

24. Muñoz-Becerra, K.; Zagal, J. H.; Venegas, R.; Recio, F. J., Strategies to improve the catalytic activity and stability of bioinspired Cu molecular catalysts for the ORR. *Current Opinion in Electrochemistry* **2022**, 101035.

25. Zhou, H.; Xiong, B.; Chen, L.; Shi, J., Modulation strategies of Cu-based electrocatalysts for efficient nitrogen reduction. *Journal of Materials Chemistry A* **2020,** *8* (39), 20286-20293.

26. Wang, X.; Qiu, S.; Feng, J.; Tong, Y.; Zhou, F.; Li, Q.; Song, L.; Chen, S.; Wu, K. H.; Su, P., Confined Fe–Cu clusters as sub-nanometer reactors for efficiently regulating the electrochemical nitrogen reduction reaction. *Advanced Materials* **2020,** *32* (40), 2004382.

27. Shan, W.; Song, H., Catalysts for the selective catalytic reduction of NO x with NH 3 at low temperature. *Catalysis Science and Technology* **2015,** *5* (9), 4280-4288.

28. Zhang, S.; Pang, L.; Chen, Z.; Ming, S.; Dong, Y.; Liu, Q.; Liu, P.; Cai, W.; Li, T., Cu/SSZ-13 and Cu/SAPO-34 catalysts for deNOx in diesel exhaust: Current status, challenges, and future perspectives. *Applied Catalysis A: General* **2020,** *607*, 117855.

29. Martín, N.; Boruntea, C. R.; Moliner, M.; Corma, A., Efficient synthesis of the Cu-SSZ-39 catalyst for DeNOx applications. *Chemical Communications* **2015,** *51* (55), 11030-11033.

30. Wang, Y.; Liu, C.; Zhang, B.; Yu, Y., Self-template synthesis of hierarchically structured Co3O4@ NiO bifunctional electrodes for selective nitrate reduction and tetrahydroisoquinolines semi-dehydrogenation. *Science. China Mater* **2020,** *63* (12), 2530-2538.

31. Manthiram, K.; Beberwyck, B. J.; Alivisatos, A. P., Enhanced electrochemical methanation of carbon dioxide with a dispersible nanoscale copper catalyst. *Journal of the American Chemical Society* **2014,** *136* (38), 13319-13325.

32. Xiaoyan, S.; Rui, W.; Dangsheng, S., Research progress in metal-free carbon-based catalysts. *Chinese Journal of Catalysis* **2013,** *34* (3), 508-523.

33. JIANG, H.-F.; WANG, Y.-G.; LIU, H.-L.; LIU, P., Application of Non-Metallic Organocatalysts in OrganicChemistry. *Chinese Journal of Organic Chemistry* **2004,** *24* (12), 1513.

34. Yang, G.; Ma, Y.; Xu, J., Biomimetic catalytic system driven by electron transfer for selective oxygenation of hydrocarbon. *Journal of the American Chemical Society* **2004,** *126* (34), 10542-10543.

35. Paradies, J., Frustrated Lewis pair catalyzed hydrogenations. *Synlett* **2013,** *24* (07), 777-780.

36. Li, W.; Wang, J.; Gong, H., Catalytic combustion of VOCs on non-noble metal catalysts. *Catalysis Today* **2009,** *148* (1-2), 81-87.

37. Li, X.; Wang, Y.; Kang, L.; Zhu, M.; Dai, B., A novel, non-metallic graphitic carbon nitride catalyst for acetylene hydrochlorination. *Journal of Catalysis* **2014,** *311*, 288-294.

38. Marinoiu, A.; Raceanu, M.; Carcadea, E.; Varlam, M.; Soare, A.; Stefanescu, I., Doped graphene as non-metallic catalyst for fuel cells. *Materials Science* **2017,** *23* (2), 108-113.

39. Mei, R.; Ma, L.; An, L.; Wang, F.; Xi, J.; Sun, H.; Luo, Z.; Wu, Q., Layered spongy-like O-doped g-C3N4: an efficient non-metal oxygen reduction catalyst for alkaline fuel cells. *Journal of The Electrochemical Society* **2017,** *164* (4), F354.

40. Nocera, D. G., Chemistry of personalized solar energy. *Inorganic Chemistry* **2009,** *48* (21), 10001-10017.

41. Cao, Y.; Yu, H.; Peng, F.; Wang, H., Selective allylic oxidation of cyclohexene catalyzed by nitrogen-doped carbon nanotubes. *American Chemistry Society Catalysis* **2014,** *4* (5), 1617-1625.

42. Waikar, J.; Pawar, H.; More, P., Review on CO oxidation by noble and non-noble metal based catalyst. *Catalysis in Green Chemistry and Engineering* **2019,** *2* (1).

43. Mestl, G.; Maksimova, N. I.; Keller, N.; Roddatis, V. V.; Schlögl, R., Carbon nanofilaments in heterogeneous catalysis: an industrial application for new carbon materials? *Angewandte Chemie International Edition* **2001,** *40* (11), 2066-2068.

44. Keller, N.; Maksimova, N. I. Roddatis, V. V,. Schur, M, Mestl, G.; Butenko, Y. V.; Kuznetsov, V. L.; Schlögl, R., The catalytic use of onion-like carbon materials for styrene synthesis by oxidative dehydrogenation of ethylbenzene. *Angewandte Chemie International Edition* **2002,** *41* (11), 1885-1888.

45. Yu, D.; Nagelli, E.; Du, F.; Dai, L., Metal-free carbon nanomaterials become more active than metal catalysts and last longer. *The Journal of Physical Chemistry Letters* **2010,** *1* (14), 2165-2173.

46. Zhu, J.; He, C.; Li, Y.; Kang, S.; Shen, P. K., One-step synthesis of boron and nitrogen-dual-self-doped graphene sheets as non-metal catalysts for oxygen reduction reaction. *Journal of Materials Chemistry A* **2013,** *1* (46), 14700-14705.

47. Li, J.; Zan, W.-Y.; Kang, H.; Dong, Z.; Zhang, X.; Lin, Y.; Mu, Y.-W.; Zhang, F.; Zhang, X.-M.; Gu, J., Graphitic-N highly doped graphene-like carbon: A superior metal-free catalyst for efficient reduction of CO2. *Applied Catalysis B: Environmental* **2021,** *298*, 120510.

48. Wang, J.; Huang, H.; Wang, P.; Wang, S.; Li, J., N, S synergistic effect in hierarchical porous carbon for enhanced NRR performance. *Carbon* **2021,** *179*, 358-364.

49. Lu, X.; Song, H.; Cai, J.; Lu, S., Recent development of electrochemical nitrate reduction to ammonia: A mini review. *Electrochemistry Communications* **2021,** *129*, 107094.

50. Figueiredo, J. L.; Pereira, M.; Freitas, M.; Orfao, J., Modification of the surface chemistry of activated carbons. *Carbon* **1999,** *37* (9), 1379-1389.

51. Figueiredo, J. L.; Pereira, M. F. R., The role of surface chemistry in catalysis with carbons. *Catalysis Today* **2010,** *150* (1-2), 2-7.

52. Légaré, M.-A.; Rochette, É.; Lavergne, J. L.; Bouchard, N.; Fontaine, F.-G., Bench-stable frustrated Lewis pair chemistry: fluoroborate salts as precatalysts for the C–H borylation of heteroarenes. *Chemical Communications* **2016,** *52* (31), 5387-5390.

53. Légaré, M.-A.; Bélanger-Chabot, G.; Dewhurst, R. D.; Welz, E.; Krummenacher, I.; Engels, B.; Braunschweig, H., Nitrogen fixation and reduction at boron. *Science* **2018,** *359* (6378), 896-900.

54. Kumar, C. V. S.; Subramanian, V., Can boron antisites of BNNTs be an efficient metal-free catalyst for nitrogen fixation?–A DFT investigation. *Physical Chemistry Chemical Physics* **2017,** *19* (23), 15377-15387.

55. Liu, C.; Li, Q.; Zhang, J.; Jin, Y.; MacFarlane, D. R.; Sun, C., Theoretical evaluation of possible 2D boron monolayer in N2 electrochemical conversion into ammonia. *The Journal of Physical Chemistry C* **2018,** *122* (44), 25268-25273.

56. Zhang, X.; Wu, T.; Wang, H.; Zhao, R.; Chen, H.; Wang, T.; Wei, P.; Luo, Y.; Zhang, Y.; Sun, X., Boron nanosheet: an elemental two-dimensional (2D) material for ambient electrocatalytic N2-to-NH3 fixation in neutral media. *American Chemistry Society Catalysis* **2019,** *9* (5), 4609-4615.

57. Mao, X.; Zhou, S.; Yan, C.; Zhu, Z.; Du, A., A single boron atom doped boron nitride edge as a metal-free catalyst for N 2 fixation. *Physical Chemistry Chemical Physics* **2019,** *21* (3), 1110-1116.

58. Cheng, N.; Zhang, L.; Doyle-Davis, K.; Sun, X., Single-atom catalysts: from design to application. *Electrochemical Energy Reviews* **2019,** *2*, 539-573.

59. Li, J.; Yue, M.-F.; Wei, Y.-M.; Li, J.-F., Synthetic strategies of single-atoms catalysts and applications in electrocatalysis. *Electrochimica Acta* **2022,** *409*, 139835.

60. Liu, L.; Corma, A., Metal catalysts for heterogeneous catalysis: from single atoms to nanoclusters and nanoparticles. *Chemical Reviews* **2018,** *118* (10), 4981-5079.

61. Nørskov, J. K.; Bligaard, T.; Hvolbæk, B.; Abild-Pedersen, F.; Chorkendorff, I.; Christensen, C. H., The nature of the active site in heterogeneous metal catalysis. *Chemical Society Reviews* **2008,** *37* (10), 2163-2171.

62. Yang, X.-F.; Wang, A.; Qiao, B.; Li, J.; Liu, J.; Zhang, T., Single-atom catalysts: a new frontier in heterogeneous catalysis. *Accounts of Chemical Research* **2013,** *46* (8), 1740-1748.

63. Kaiser, S. K.; Chen, Z.; Faust Akl, D.; Mitchell, S.; Perez-Ramirez, J., Single-atom catalysts across the periodic table. *Chemical Reviews* **2020,** *120* (21), 11703-11809.

64. Chen, Y.; Ji, S.; Chen, C.; Peng, Q.; Wang, D.; Li, Y., Single-atom catalysts: synthetic strategies and electrochemical applications. *Joule* **2018,** *2* (7), 1242-1264.

65. Lang, R.; Du, X.; Huang, Y.; Jiang, X.; Zhang, Q.; Guo, Y.; Liu, K.; Qiao, B.; Wang, A.; Zhang, T., Single-atom catalysts based on the metal–oxide interaction. *Chemical Reviews* **2020,** *120* (21), 11986-12043.

66. Qiao, B.; Wang, A.; Yang, X.; Allard, L. F.; Jiang, Z.; Cui, Y.; Liu, J.; Li, J.; Zhang, T., Single-atom catalysis of CO oxidation using Pt1/FeO x. *Nature Chemistry* **2011,** *3* (8), 634-641.

67. He, W.-L.; Yang, X.-L.; Zhao, M.; Wu, C.-D., Suspending ionic single-atom catalysts in porphyrinic frameworks for highly efficient aerobic oxidation at room temperature. *Journal of Catalysis* **2018,** *358*, 43-49.

68. Li, M.; Wu, S.; Yang, X.; Hu, J.; Peng, L.; Bai, L.; Huo, Q.; Guan, J., Highly efficient single atom cobalt catalyst for selective oxidation of alcohols. *Applied Catalysis A: General* **2017,** *543*, 61-66.

69. Sharma, R. K.; Dutta, S.; Sharma, S.; Zboril, R.; Varma, R. S.; Gawande, M. B., Fe 3 O 4 (iron oxide)-supported nanocatalysts: synthesis, characterization and applications in coupling reactions. *Green Chemistry* **2016,** *18* (11), 3184-3209.

70. Gawande, M. B.; Fornasiero, P.; Zbořil, R., Carbon-based single-atom catalysts for advanced applications. *American Chemistry Society Catalysis* **2020,** *10* (3), 2231-2259.

71. Chen, Z.; Vorobyeva, E.; Mitchell, S.; Fako, E.; Ortuño, M. A.; López, N.; Collins, S. M.; Midgley, P. A.; Richard, S.; Vilé, G., A heterogeneous single-atom palladium catalyst surpassing homogeneous systems for Suzuki coupling. *Nature Nanotechnology* **2018,** *13* (8), 702-707.

72. Shen, M.; Wei, C.; Ai, K.; Lu, L., Transition metal–nitrogen–carbon nanostructured catalysts for the oxygen reduction reaction: from mechanistic insights to structural optimization. *Nano Research* **2017,** *10*, 1449-1470.

73. Li, M.; Wang, H.; Luo, W.; Sherrell, P. C.; Chen, J.; Yang, J., Heterogeneous single-atom catalysts for electrochemical CO2 reduction reaction. *Advanced Materials* **2020,** *32* (34), 2001848.

74. Xue, Z.; Zhang, X.; Qin, J.; Liu, R., High-throughput identification of high activity and selectivity transition metal single-atom catalysts for nitrogen reduction. *Nano Energy* **2021,** *80*, 105527.

75. Zheng, T.; Jiang, K.; Ta, N.; Hu, Y.; Zeng, J.; Liu, J.; Wang, H., Large-scale and highly selective CO2 electrocatalytic reduction on nickel single-atom catalyst. *Joule* **2019,** *3* (1), 265-278.

76. Zhang, H.; Li, J.; Xi, S.; Du, Y.; Hai, X.; Wang, J.; Xu, H.; Wu, G.; Zhang, J.; Lu, J., A graphene-supported single-atom FeN5 catalytic site for efficient electrochemical CO2 reduction. *Angewandte Chemie* **2019,** *131* (42), 15013-15018.

77. Wang, M.; Liu, S.; Qian, T.; Liu, J.; Zhou, J.; Ji, H.; Xiong, J.; Zhong, J.; Yan, C., Over 56.55% Faradaic efficiency of ambient ammonia synthesis enabled by positively shifting the reaction potential. *Nature Communications* **2019,** *10* (1), 341.

78. Han, L.; Liu, X.; Chen, J.; Lin, R.; Liu, H.; Lü, F.; Bak, S.; Liang, Z.; Zhao, S.; Stavitski, E., Atomically dispersed molybdenum catalysts for efficient ambient nitrogen fixation. *Angewandte Chemie* **2019,** *131* (8), 2343-2347.

79. Chen, G.-F.; Yuan, Y.; Jiang, H.; Ren, S.-Y.; Ding, L.-X.; Ma, L.; Wu, T.; Lu, J.; Wang, H., Electrochemical reduction of nitrate to ammonia via direct eight-electron transfer using a copper–molecular solid catalyst. *Nature Energy* **2020,** *5* (8), 605-613.

80. Li, T.; Wu, Y.; Pei, M., Screening of transition metal single-atom catalysts doped on γ-graphyne-like BN sheet for efficient nitrogen reduction reaction. *Journal of Alloys and Compounds* **2022,** *908*, 164675.

81. Ji, S.; Chen, Y.; Wang, X.; Zhang, Z.; Wang, D.; Li, Y., Chemical synthesis of single atomic site catalysts. *Chemical Reviews* **2020,** *120* (21), 11900-11955.

82. Gao, J.; Liu, B., Progress of electrochemical hydrogen peroxide synthesis over single atom catalysts. *American Chemistry Society Materials Letters* **2020,** *2* (8), 1008-1024.

83. Yang, Y.; Yang, Y.; Pei, Z.; Wu, K.-H.; Tan, C.; Wang, H.; Wei, L.; Mahmood, A.; Yan, C.; Dong, J., Recent progress of carbon-supported single-atom catalysts for energy conversion and storage. *Matter* **2020,** *3* (5), 1442-1476.

84. Zhao, S.; Cheng, Y.; Veder, J.-P.; Johannessen, B.; Saunders, M.; Zhang, L.; Liu, C.; Chisholm, M. F.; De Marco, R.; Liu, J., One-pot pyrolysis method to fabricate carbon nanotube supported Ni single-atom catalysts with ultrahigh loading. *American Chemistry Society Applied Energy Materials* **2018,** *1* (10), 5286-5297.

85. Cheng, Y.; He, S.; Lu, S.; Veder, J. P.; Johannessen, B.; Thomsen, L.; Saunders, M.; Becker, T.; De Marco, R.; Li, Q., Iron single atoms on graphene as nonprecious metal catalysts for high-temperature polymer electrolyte membrane fuel cells. *Advanced Science* **2019,** *6* (10), 1802066.

86. Wang, J.; Yu, L.; Hu, L.; Chen, G.; Xin, H.; Feng, X., Ambient ammonia synthesis via palladium-catalyzed electrohydrogenation of dinitrogen at low overpotential. *Nature Communications* **2018,** *9* (1), 1795.

87. Qiu, W.; Xie, X.-Y.; Qiu, J.; Fang, W.-H.; Liang, R.; Ren, X.; Ji, X.; Cui, G.; Asiri,A. M.; Cui, G., High-performance artificial nitrogen fixation at ambient conditions using a metal-free electrocatalyst. *Nature Communications* **2018,** *9* (1), 3485.

88. Geng, Z.; Liu, Y.; Kong, X.; Li, P.; Li, K.; Liu, Z.; Du, J.; Shu, M.; Si, R.; Zeng, J., Achieving a record-high yield rate of 120.9 for N2 electrochemical reduction over Ru single-atom catalysts. *Advanced Materials* **2018,** *30* (40), 1803498.

89. Wang, C.; Zhou, W.; Sun, Z.; Wang, Y.; Zhang, B.; Yu, Y., Integrated selective nitrite reduction to ammonia with tetrahydroisoquinoline semi-dehydrogenation over a vacancy-rich Ni bifunctional electrode. *Journal of Materials Chemistry A* **2021,** *9* (1), 239-243.

90. Brown, K. A.; Harris, D. F.;Wilker, M. B.; Rasmussen, A.; Khadka, N.; Hamby, H.; Keable, S.; Dukovic, G.; Peters, J. W.; Seefeldt, L. C., Light-driven dinitrogen reduction catalyzed by a CdS: nitrogenase MoFe protein biohybrid. *Science* **2016,** *352* (6284), 448-450.

91. Chang, C.; Chen, W.; Chen, Y.; Chen, Y.; Chen, Y.; Ding, F.; Fan, C.; Fan, H. J.; Fan, Z.; Gong, C., Recent progress on two-dimensional materials. *Acta Physico-Chimica Sinica* **2021,** *37* (12), 2108017.

92. Huang, P.; Fan, T.; Ma, X.; Zhang, J.; Zhang, Y.; Chen, Z.; Yi, X., 3D Flower-Like Zinc Cobaltite for Electrocatalytic Reduction of Nitrate to Ammonia under Ambient Conditions. *ChemSusChem* **2022,** *15* (4), e202102049.

93. Yang, J.; Qi, H.; Li, A.; Liu, X.; Yang, X.; Zhang, S.; Zhao, Q.; Jiang, Q.; Su, Y.;Zhang, L., Potential-driven restructuring of Cu single atoms to nanoparticles for boosting the electrochemical reduction of nitrate to ammonia. *Journal of the American Chemical Society* **2022,** *144* (27), 12062-12071.

94. Wang, L.; Xia, M.; Wang, H.; Huang, K.; Qian, C.; Maravelias, C. T.; Ozin, G. A., Greening ammonia toward the solar ammonia refinery. *Joule* **2018,** *2* (6), 1055-1074.

95. Erismann, J.; Sutton, M.; Gallowaz, J.; Klimont, Y.; Winiwarter, W., How a century of ammonia synthesis changed the world. *Nature Geoscience* **2008,** *1*, 636-639.

96. Hu, H.; Yang, H.; Yang, X.; Wang, R.; Zhou, L.; Dai, Y.; Ji, N.; Wang, H.; Shi, Z.; Zhou, G., Copper-sulfide cluster assembled architecture via in situ reaction. *Chinese Chemical Letters* **2020,** *31* (12), 3213-3215.

97. Chen, J. G.; Crooks, R. M.; Seefeldt, L. C.; Bren, K. L.; Bullock, R. M.; Darensbourg, M. Y.; Holland, P. L.; Hoffman, B.; Janik, M. J.; Jones, A. K., Beyond fossil fuel–driven nitrogen transformations. *Science* **2018,** *360* (6391), eaar6611.

98. Ahlgren, W. L., The dual-fuel strategy: an energy transition plan. *Proceedings of the IEEE* **2012,** *100* (11), 3001-3052.

99. Wang, H.; Huang, B.; Yu, C.; Lu, M.; Huang, H.; Zhou, Y., Research progress, challenges and perspectives on the sulfur and water resistance of catalysts for low temperature selective catalytic reduction of NOx by NH3. *Applied Catalysis A: General* **2019,** *588*, 117207.

100. Rafiqul, I.; Weber, C.; Lehmann, B.; Voss, A., Energy efficiency improvements in ammonia production—perspectives and uncertainties. *Energy* **2005,** *30* (13), 2487-2504.

101. Elvers, B., *Ullmann's encyclopedia of industrial chemistry*. Verlag Chemie Hoboken, NJ: 1991; Vol. 17.

102. Patil, B.; Wang, Q.; Hessel, V.; Lang, J., Plasma N2-fixation: 1900–2014. *Catalysis Today* **2015,** *256*, 49-66.

103. Zhao, C.; Xi, M.; Huo, J.; He, C.; Fu, L., Electro-reduction of N2 on nanostructured materials and the design strategies of advanced catalysts based on descriptors. *Materials Today Physics* **2022**, 100609.

104. Chen, Q.; Zhang, X.; Jin, Y.; Zhou, X.; Yang, Z.; Nie, H., An Overview on Noble Metal (Group VIII)-based Heterogeneous Electrocatalysts for Nitrogen Reduction Reaction. *Chemistry–An Asian Journal* **2020,** *15* (24), 4131-4152.

105. Xiang, Z.; Li, L.; Wang, Y.; Song, Y., Recent Advances in Noble-Metal-Free Catalysts for Electrocatalytic Synthesis of Ammonia under Ambient Conditions. *Chemistry–An Asian Journal* **2020,** *15* (12), 1791-1807.

106. Shi, M. M.; Bao, D.; Wulan, B. R.; Li, Y. H.; Zhang, Y. F.; Yan, J. M.; Jiang, Q., Au sub-nanoclusters on TiO2 toward highly efficient and selective electrocatalyst for N2 conversion to NH3 at ambient conditions. *Advanced Materials* **2017,** *29* (17), 1606550.

107. Jia, H.-P.; Quadrelli, E. A., Mechanistic aspects of dinitrogen cleavage and hydrogenation to produce ammonia in catalysis and organometallic chemistry: relevance of metal hydride bonds and dihydrogen. *Chemical Society Reviews* **2014,** *43* (2), 547-564.

108. Yuan, M.; Zhang, H.; Gao, D.; He, H.; Sun, Y.; Lu, P.; Dipazir, S.; Li, Q.; Zhou, L.; Li, S., Support effect boosting the electrocatalytic N 2 reduction activity of Ni 2 P/N, P-codoped carbon nanosheet hybrids. *Journal of Materials Chemistry A* **2020,** *8* (5), 2691-2700.

109. Han, Y.; Wang, Y.; Ma, T.; Li, W.; Zhang, J.; Zhang, M., Mechanistic understanding of Cu-based bimetallic catalysts. *Frontiers of Chemical Science and Engineering* **2020,** *14*, 689-748.

110. Chopra, N. G.; Luyken, R.; Cherrey, K.; Crespi, V. H.; Cohen, M. L.; Louie, S. G.; Zettl, A., Boron nitride nanotubes. *Science* **1995,** *269* (5226), 966-967.

111. Weng, Q.; Wang, X.; Bando, Y.; Golberg, D., One-step template-free synthesis of highly porous boron nitride microsponges for hydrogen storage. *Advanced Energy Materials* **2014,** *4* (7), 1301525.

112. Marchesini, S.; McGilvery, C. M.; Bailey, J.; Petit, C., Template-free synthesis of highly porous boron nitride: insights into pore network design and impact on gas sorption. *ACS nano* **2017,** *11* (10), 10003-10011.

113. Yao, Z.; Hu, M.; Iqbal, Z.; Wang, X., N8–polynitrogen stabilized on boron-doped graphene as metal-free electrocatalysts for oxygen reduction reaction. *Americna Chemistry Society Catalysis* **2019,** *10* (1), 160-167.

114. Niedzielski, P.; Kurzyca, I.; Siepak, J., A new tool for inorganic nitrogen speciation study: Simultaneous determination of ammonium ion, nitrite and nitrate by ion chromatography with post-column ammonium derivatization by Nessler reagent and diode-array detection in rain water samples. *Analytica Chimica Acta* **2006,** *577* (2), 220-224.

115. Jeong, H.; Park, J.; Kim, H., Determination of NH4+ in environmental water with interfering substances using the modified Nessler method. *Journal of Chemistry* **2013,** *2013*.

116. Liu, C.; Li, Q.; Wu, C.; Zhang, J.; Jin, Y.; MacFarlane, D. R.; Sun, C., Single-boron catalysts for nitrogen reduction reaction. *Journal of the American Chemical Society* **2019,** *141* (7), 2884-2888.

117. Chang, B.; Li, L.; Shi, D.; Jiang, H.; Ai, Z.; Wang, S.; Shao, Y.; Shen, J.; Wu, Y.; Li, Y., Metal-free boron carbonitride with tunable boron Lewis acid sites for enhanced nitrogen electroreduction to ammonia. *Applied Catalysis B: Environmental* **2021,** *283*, 119622.

118. Ko, B. H.; Hasa, B.; Shin, H.; Zhao, Y.; Jiao, F., Electrochemical reduction of gaseous nitrogen oxides on transition metals at ambient conditions. *Journal of the American Chemical Society* **2022,** *144* (3), 1258-1266.

119. Elzey, S.; Baltrusaitis, J.; Bian, S.; Grassian, V. H., Formation of paratacamite nanomaterials via the conversion of aged and oxidized copper nanoparticles in hydrochloric acidic media. *Journal of Materials Chemistry* **2011,** *21* (9), 3162-3169.

120. Li, L.; Tang, C.; Cui, X.; Zheng, Y.; Wang, X.; Xu, H.; Zhang, S.; Shao, T.; Davey, K.; Qiao, S. Z., Efficient nitrogen fixation to ammonia through integration of plasma oxidation with electrocatalytic reduction. *Angewandte Chemie* **2021,** *133* (25), 14250-14256.

121. Liang, J.; Liu, Q.; Alshehri, A. A.; Sun, X., Recent advances in nanostructured heterogeneous catalysts for N-cycle electrocatalysis. *Nano Research Energy* **2022,** *1* (2), e9120010.

122. Yang, X.; Kattel, S.; Nash, J.; Chang, X.; Lee, J. H.; Yan, Y.; Chen, J. G.; Xu, B., Quantification of active sites and elucidation of the reaction mechanism of the electrochemical nitrogen reduction reaction on vanadium nitride. *Angewandte Chemie International Edition* **2019,** *58* (39), 13768-13772.

123. Wang, Y.; Yu, Y.; Jia, R.; Zhang, C.; Zhang, B., Electrochemical synthesis of nitric acid from air and ammonia through waste utilization. *National Science Review* **2019,** *6* (4), 730-738.

124. Wang, X.; Wang, W.; Qiao, M.; Wu, G.; Chen, W.; Yuan, T.; Xu, Q.; Chen, M.; Zhang, Y.; Wang, X., Atomically dispersed Au1 catalyst towards efficient electrochemical synthesis of ammonia. *Science Bulletin* **2018,** *63* (19), 1246-1253.

125. Organization, W. H., A global overview of national regulations and standards for drinking-water quality. **2021 02**.

126. Fang, L.; Wang, S.; Song, C.; Lu, S.; Yang, X.; Qi, X.; Liu, H., Boosting nitrate electroreduction to ammonia via in situ generated stacking faults in oxide-derived copper. *Chemical Engineering Journal* **2022,** *446*, 137341.

127. Lin, S.; Zhang, X.; Chen, L.; Zhang, Q.; Ma, L.; Liu, J., A review on catalysts for electrocatalytic and photocatalytic reduction of N2 to ammonia. *Green Chemistry* **2022**.

128. Suryanto, B. H.; Du, H.-L.; Wang, D.; Chen, J.; Simonov, A. N.; MacFarlane, D. R., Challenges and prospects in the catalysis of electroreduction of nitrogen to ammonia. *Nature Catalysis* **2019,** *2* (4), 290-296.

129. Teng, M.; Ye, J.; Wan, C.; He, G.; Chen, H., Research Progress on Cu-Based Catalysts for Electrochemical Nitrate Reduction Reaction to Ammonia. *Industrial & Engineering Chemistry Research* **2022,** *61* (40), 14731-14746.

130. Fu, X.; Zhao, X.; Hu, X.; He, K.; Yu, Y.; Li, T.; Tu, Q.; Qian, X.; Yue, Q.; Wasielewski, M. R., Alternative route for electrochemical ammonia synthesis by reduction of nitrate on copper nanosheets. *Applied Materials Today* **2020,** *19*, 100620.

131. Zang, W.; Yang, T.; Zou, H.; Xi, S.; Zhang, H.; Liu, X.; Kou, Z.; Du, Y.; Feng, Y. P.; Shen, L., Copper single atoms anchored in porous nitrogen-doped carbon as efficient pH-universal catalysts for the nitrogen reduction reaction. *American Chemistry Society Catalysis* **2019,** *9* (11), 10166-10173.

132. Zhu, T.; Chen, Q.; Liao, P.; Duan, W.; Liang, S.; Yan, Z.; Feng, C., Single-atom Cu catalysts for enhanced electrocatalytic nitrate reduction with significant alleviation of nitrite production. *Small* **2020,** *16* (49), 2004526.

133. Lomachenko, K. A.; Borfecchia, E.; Negri, C.; Berlier, G.; Lamberti, C.; Beato, P.; Falsig, H.; Bordiga, S., The Cu-CHA deNO x catalyst in action: temperature-dependent NH3-assisted selective catalytic reduction monitored by operando XAS and XES. *Journal of the American Chemical Society* **2016,** *138* (37), 12025-12028.

134. Huan, T. N.; Andreiadis, E. S.; Heidkamp, J.; Simon, P.; Derat, E.; Cobo, S.; Royal, G.; Bergmann, A.; Strasser, P.; Dau, H., From molecular copper complexes to composite electrocatalytic materials for selective reduction of CO2 to formic acid. *Journal of Materials Chemistry A* **2015,** *3* (7), 3901-3907.

135. Lytle, F. W.; Greegor, R. B.; Panson, A. J., Discussion of X-ray-absorption near-edge structure: Application to Cu in the high-T c superconductors La 1.8 Sr 0.2 CuO 4 and YBa 2 Cu 3 O 7. *Physical Review B* **1988,** *37* (4), 1550.

136. Liu, H.; Lang, X.; Zhu, C.; Timoshenko, J.; Rüscher, M.; Bai, L.; Guijarro, N.; Yin, H.; Peng, Y.; Li, J., Efficient Electrochemical Nitrate Reduction to Ammonia with Copper-Supported Rhodium Cluster and Single-Atom Catalysts. *Angewandte Chemie* **2022**, e202202556.

137. Abdel-Mageed, A. M.; Rungtaweevoranit, B.; Parlinska-Wojtan, M.; Pei, X.; Yaghi, O. M.; Behm, R. J. r., Highly active and stable single-atom Cu catalysts supported by a metal–organic framework. *Journal of the American Chemical Society* **2019,** *141* (13), 5201-5210.

138. Beale, A. M.; Gao, F.; Lezcano-Gonzalez, I.; Peden, C. H.; Szanyi, J., Recent advances in automotive catalysis for NO x emission control by small-pore microporous materials. *Chemical Society Reviews* **2015,** *44* (20), 7371-7405.

139. Borfecchia, E.; Lomachenko, K.; Giordanino, F.; Falsig, H.; Beato, P.; Soldatov, A.; Bordiga, S.; Lamberti, C., Revisiting the nature of Cu sites in the activated Cu-SSZ-13 catalyst for SCR reaction. *Chemical Science* **2015,** *6* (1), 548-563.

140. Yang, L.-F.; Qin, H.-G.; Li, F.-Z.; Peng, J.-Z.; Gu, J., Cation modified Fe–N–C catalyst for the electrochemical reduction of nitrate in solutions of low ionic strength. *Inorganic Chemistry Frontiers* **2023**.

141. Xu, Y.; Wang, M.; Ren, K.; Ren, T.; Liu, M.; Wang, Z.; Li, X.; Wang, L.; Wang, H., Atomic defects in pothole-rich two-dimensional copper nanoplates triggering enhanced electrocatalytic selective nitrate-to-ammonia transformation. *Journal of Materials Chemistry A* **2021,** *9* (30), 16411-16417.

142. Reyter, D.; Belanger, D.; Roue, L., Elaboration of Cu−Pd films by coelectrodeposition: application to nitrate electroreduction. *The Journal of Physical Chemistry C* **2009,** *113* (1), 290-297.

143. Anastasopoulos, A.; Hannah, L.; Hayden, B. E., High throughput optimisation of PdCu alloy electrocatalysts for the reduction of nitrate ions. *Journal of Catalysis* **2013,** *305*, 27-35.

144. Gootzen, J.; Peeters, P.; Dukers, J.; Lefferts, L.; Visscher, W.; Van Veen, J., The electrocatalytic reduction of NO3− on Pt, Pd and Pt+ Pd electrodes activated with Ge. *Journal of Electroanalytical Chemistry* **1997,** *434* (1-2), 171-183.

145. Taguchi, S.; Feliu, J. M., Kinetic study of nitrate reduction on Pt (1 1 0) electrode in perchloric acid solution. *Electrochimica Acta* **2008,** *53* (10), 3626-3634.

146. Abdallah, R.; Geneste, F.; Labasque, T.; Djelal, H.; Fourcade, F.; Amrane, A.; Taha, S.; Floner, D., Selective and quantitative nitrate electroreduction to ammonium using a porous copper electrode in an electrochemical flow cell. *Journal of Electroanalytical Chemistry* **2014,** *727*, 148-153.

147. Comisso, N.; Cattarin, S.; Guerriero, P.; Mattarozzi, L.; Musiani, M.; Vázquez-Gómez, L.; Verlato, E., Study of Cu, Cu-Ni and Rh-modified Cu porous layers as electrode materials for the electroanalysis of nitrate and nitrite ions. *Journal of Solid State Electrochemistry* **2016,** *20* (4), 1139-1148.

148. Li, M.; Sun, Y. Z.; Li, C. Y.; Wan, P. Y. In *Electrochemical reduction of nitrate by Fe-Si alloy electrode*, Advanced Materials Research, Trans Tech Publ: 2011; pp 1789-1794.

149. Li, J.; Zhan, G.; Yang, J.; Quan, F.; Mao, C.; Liu, Y.; Wang, B.; Lei, F.; Li, L.; Chan, A. W., Efficient ammonia electrosynthesis from nitrate on strained ruthenium nanoclusters. *Journal of the American Chemical Society* **2020,** *142* (15), 7036-7046.

150. Liu, H.; Park, J.; Chen, Y.; Qiu, Y.; Cheng, Y.; Srivastava, K.; Gu, S.; Shanks, B. H.; Roling, L. T.; Li, W., Electrocatalytic nitrate reduction on oxide-derived silver with tunable selectivity to nitrite and ammonia. *American Chemistry Society Catalysis* **2021,** *11* (14), 8431-8442.

151. Deng, X.; Yang, Y.; Wang, L.; Fu, X. Z.; Luo, J. L., Metallic Co nanoarray catalyzes selective NH3 production from electrochemical nitrate reduction at current densities exceeding 2 A cm− 2. *Advanced Science* **2021,** *8* (7), 2004523.

152. Teng, W.; Bai, N.; Liu, Y.; Liu, Y.; Fan, J.; Zhang, W.-x., Selective nitrate reduction to dinitrogen by electrocatalysis on nanoscale iron encapsulated in mesoporous carbon. *Environmental Science and Technology* **2018,** *52* (1), 230-236.

153. Reyter, D.; Bélanger, D.; Roué, L., Optimization of the cathode material for nitrate removal by a paired electrolysis process. *Journal of Hazardous Materials* **2011,** *192* (2), 507-513.

154. Roy, C.; Deschamps, J.; Martin, M.; Bertin, E.; Reyter, D.; Garbarino, S.; Roué, L.; Guay, D., Identification of Cu surface active sites for a complete nitrate-to-nitrite conversion with nanostructured catalysts. *Applied Catalysis B: Environmental* **2016,** *187*, 399-407.

155. Wang, Y.; Zhou, W.; Jia, R.; Yu, Y.; Zhang, B., Unveiling the activity origin of a copper-based electrocatalyst for selective nitrate reduction to ammonia. *Angewandte Chemie International edition* **2020,** *59* (13), 5350-5354.

156. Xiao, Z.; Huang, Y.-C.; Dong, C.-L.; Xie, C.; Liu, Z.; Du, S.; Chen, W.; Yan, D.; Tao, L.; Shu, Z., Operando identification of the dynamic behavior of oxygen vacancy-rich Co3O4 for oxygen evolution reaction. *Journal of the American Chemical Society* **2020,** *142* (28), 12087-12095.

157. Zhu, Y.; He, Z.; Choi, Y.; Chen, H.; Li, X.; Zhao, B.; Yu, Y.; Zhang, H.; Stoerzinger, K. A.; Feng, Z., Tuning proton-coupled electron transfer by crystal orientation for efficient water oxidization on double perovskite oxides. *Nature Communications* **2020,** *11* (1), 4299.

158. Zhou, Q.; Zhang, W.; Qiu, M.; Yu, Y., Role of oxygen in copper-based catalysts for carbon dioxide electrochemical reduction. *Materials Today Physics* **2021,** *20*, 100443.

159. De Gregorio, G. L.; Burdyny, T.; Loiudice, A.; Iyengar, P.; Smith, W. A.; Buonsanti, R., Facet-dependent selectivity of Cu catalysts in electrochemical CO2 reduction at commercially viable current densities. *American Chemistry Society Catalysis* **2020,** *10* (9), 4854-4862.

160. Liu, C.-j.; Vissokov, G. P.; Jang, B. W.-L., Catalyst preparation using plasma technologies. *Catalysis Today* **2002,** *72* (3-4), 173-184.

161. Cherednichenko, K. A.; Le Godec, Y.; Kalinko, A.; Mezouar, M.; Solozhenko, V. L., Orthorhombic boron oxide under pressure: In situ study by X-ray diffraction and Raman scattering. *Journal of Applied Physics* **2016,** *120* (17), 175901.

162. Harrison, H.; Lamb, J. T.; Nowlin, K. S.; Guenthner, A. J.; Ghiassi, K. B.; Kelkar, A. D.; Alston, J. R., Quantification of hexagonal boron nitride impurities in boron nitride nanotubes via FTIR spectroscopy. *Nanoscale Advances* **2019,** *1* (5), 1693-1701.

163. Shin, W. G.; Calder, S.; Ugurlu, O.; Girshick, S. L., Production and characterization of boron nanoparticles synthesized with a thermal plasma system. *Journal of Nanoparticle Research* **2011,** *13*, 7187-7191.

164. Chu, S.; Li, X.; Prins, R.; Wang, C.; Liu, Y.; Wang, A.; Sheng, Q., Preparation of ultrasmall Ni2P nanoparticles with low P/Ni ratios supported on SiO2 and an Al2O3-B2O3 mixed oxide for dibenzothiophene hydrodesulfurization. *Journal of Catalysis* **2023**.

165. Zhang, L.; Fan, G.; Xu, W.; Yu, M.; Wang, L.; Yan, Z.; Cheng, F., Isolated diatomic Zn–Fe in N-doped carbon for electrocatalytic nitrogen reduction to ammonia. *Chemical Communications* **2020,** *56* (80), 11957-11960.

166. Han, L.; Ren, Z.; Ou, P.; Cheng, H.; Rui, N.; Lin, L.; Liu, X.; Zhuo, L.; Song, J.; Sun, J., Modulating single-atom palladium sites with copper for enhanced ambient ammonia electrosynthesis. *Angewandte Chemie* **2021,** *133* (1), 349-354.